

**CONCENTRATOR PHOTOVOLTAIC SYSTEM:
OPTICAL CHARACTERISATION**

NG JUIN LERG

**A project report submitted in partial fulfilment of the
requirements for the award of Bachelor of Engineering
(Honours) Electrical and Electronic Engineering**

**Lee Kong Chian Faculty of Engineering and Science
Universiti Tunku Abdul Rahman**

September 2020

DECLARATION

I hereby declare that this project report is based on my original work except for citations and quotations which have been duly acknowledged. I also declare that it has not been previously and concurrently submitted for any other degree or award at UTAR or other institutions.

Signature : **NG**

Name : NG JUIN LERG

ID No. : 16UEB00379

Date : 10/9/2020

APPROVAL FOR SUBMISSION


I certify that this project report entitled “**CONCENTRATOR PHOTOVOLTAIC SYSTEM: OPTICAL CHARACTERISATION**” was prepared by **NG JUIN LERG** has met the required standard for submission in partial fulfilment of the requirements for the award of Bachelor of Engineering (Honours) Electrical and Electronic Engineering at Universiti Tunku Abdul Rahman.

Approved by,

Signature : K.K.Chong

Supervisor : Prof Dr Chong Kok Keong

Date : 10/9/2020

Signature : 

Co-Supervisor : Ir. Dr. Chuah Yea Dat

Date : 11/9/2020

The copyright of this report belongs to the author under the terms of the copyright Act 1987 as qualified by Intellectual Property Policy of Universiti Tunku Abdul Rahman. Due acknowledgement shall always be made of the use of any material contained in, or derived from, this report.

© 2020, Ng Juin Lerg. All right reserved.

ACKNOWLEDGEMENTS

I would like to express my gratitude to everyone who had contributed to the successful completion of this project. A special thanks to my research supervisor, Prof. Dr. Chong Kok Keong for providing guidance and being very understanding while this research was being carried out during this difficult MCO period.

In addition, I would also like to express my gratitude to my loving parents and friends who had given me encouragement and motivation that brought this project to fruition.

ABSTRACT

In this study, the optical characteristics of an ultra-high concentrator photovoltaic (UHCPV) system such as the uniformity of flux distribution, spillage loss, solar concentration ratio (SCR), tolerance angle against sun-tracking error, tolerance length against focal distance deviation and tolerance angle against slope error of NIDC quadrant have been explored using the ray-tracing software TracePro. In the simulation, the UHCPV system has a primary optical element (POE) consisting of 480 facet mirrors forming the non-imaging dish concentrator (NIDC) and a secondary optical element (SOE) consisting of a 2×2 array of B270 Schott glass crossed compound parabolic concentrator (CCPC). The NIDC can focus the sunlight into a uniformly illuminated area of $30 \text{ mm} \times 30 \text{ mm}$ with a solar concentration ratio (SCR) of 525 suns while the CCPC can further concentrate the sunlight into 2367.85 suns at its exit aperture. The optimum receiver area is determined to be $60 \text{ mm} \times 60 \text{ mm}$ with a spillage loss 11.8%. The results are then compared to the work done by Wong et al. (2017) and deemed to be sufficiently close. In addition, the tolerance angle against sun-tracking error of the UHCPV system that receives at least 95% of energy is found to be as 0.44° . The tolerance length against focal distance deviation is 10 mm which results in less than 5% of energy loss compared to an ideal focal distance of 1200 mm. Also, the tolerance angle against slope error of NIDC quadrant that receives at least 95% of energy is obtained as 0.3° for the case of single quadrant tilting and two adjacent quadrant tilting while 0.22° is the tolerance angle for the case of two diagonal quadrant tilting.

TABLE OF CONTENTS

| | | |
|--|--|-------------|
| DECLARATION | | ii |
| APPROVAL FOR SUBMISSION | | iii |
| ACKNOWLEDGEMENTS | | v |
| ABSTRACT | | vi |
| TABLE OF CONTENTS | | i |
| LIST OF TABLES | | iv |
| LIST OF FIGURES | | v |
| LIST OF SYMBOLS / ABBREVIATIONS | | viii |
| CHAPTER | | |
| 1 | INTRODUCTION | 1 |
| | 1.1 General Introduction | 1 |
| | 1.2 Importance of the Study | 3 |
| | 1.3 Problem Statement | 3 |
| | 1.4 Aim and Objectives | 4 |
| | 1.5 Scope and Limitation of the Study | 4 |
| | 1.6 Contribution of the Study | 5 |
| | 1.7 Outline of the Report | 5 |
| 2 | LITERATURE REVIEW | 6 |
| | 2.1 Introduction | 6 |
| | 2.2 Literature Review | 6 |
| | 2.2.1 Overview of Concentrator Photovoltaic (CPV) | 6 |
| | 2.2.2 Components in CPV and Specific Design Requirements | 9 |
| | 2.2.3 Developmental Trends in CPV Technology | 12 |
| | 2.2.4 Work Done by Wong et al. (2017) and Chong et al. (2017) | 13 |
| | 2.2.5 Effect of Non-Uniform Illumination on the Performance of CPV | 13 |
| | 2.2.6 Effect of Temperature on the Performance of CPV | 14 |
| | 2.3 Summary | 14 |

| | | |
|----------|---|-----------|
| 3 | METHODOLOGY AND WORK PLAN | 15 |
| 3.1 | Introduction | 15 |
| 3.2 | System description | 15 |
| 3.3 | Ray tracing simulation | 17 |
| | 3.3.1 SCR on the receiver area at 1200 mm focal distance | 17 |
| | 3.3.2 Spillage loss | 17 |
| | 3.3.3 Comparison with the results of Wong et al. (2017) | 17 |
| | 3.3.4 System performance with sun-tracking error | 18 |
| | 3.3.5 System performance with focal distance deviation | 18 |
| | 3.3.6 System performance with slope error of NIDC quadrant | 19 |
| 3.4 | Summary | 20 |
| 4 | RESULTS AND DISCUSSION | 22 |
| 4.1 | Introduction | 22 |
| 4.2 | SCR on the receiver area at 1200 mm focal distance | 22 |
| 4.3 | Spillage loss | 23 |
| 4.4 | SCR at exit aperture of CCPC | 24 |
| 4.5 | Comparison of results to work done by Wong et al. (2017) | 26 |
| 4.6 | System performance with sun-tracking error | 27 |
| 4.7 | System performance with focal distance deviation | 33 |
| 4.8 | System performance with slope error of a NIDC quadrant | 36 |
| | 4.8.1 Single quadrant tilted with respect to x-axis and y-axis | 36 |
| | 4.8.2 Two adjacent quadrants tilted with respect to x-axis | 38 |
| | 4.8.3 Two diagonal quadrants tilted with respect to x-axis and y-axis | 40 |
| | 4.8.4 Tolerance angle against slope error | 41 |

| | | |
|----------|--|-----------|
| 5 | CONCLUSIONS AND RECOMMENDATIONS | 43 |
| 5.1 | Conclusions | 43 |
| 5.2 | Recommendations for future work | 44 |
| | REFERENCES | 45 |

LIST OF TABLES

| | |
|---|----|
| Table 2.1: The pros and cons of CPV (Philipps et al., 2015, p. 9). | 7 |
| Table 4.1: Characteristics of solar flux distribution for different tracking errors including 0° , 0.2° , 0.4° , 0.6° , 0.8° and 1° with a focal distance of 1200 mm. | 30 |
| Table 4.2: Characteristics of solar flux distribution at the 4 CCPC lens at focal distance from 1150 mm to 1250 mm. | 33 |

LIST OF FIGURES

| | |
|---|----|
| Figure 2.1: Defining focal distance, f , half opening angle, θ and indicating the input position of solar power, $P_{aperture}$ and $P_{flux, cell}$. | 9 |
| Figure 2.2: Summary of the technologies, methods and materials used to design III-V MJSC. | 11 |
| Figure 2.3: Development of efficiencies of III-V multi-junction solar cells and CPV modules. | 12 |
| Figure 3.1: Schematic diagram of UHCPV system. | 16 |
| Figure 3.2: Cross-sectional view of CCPC lens. | 16 |
| Figure 3.3: TracePro modelling of the UHCPV system. | 16 |
| Figure 3.4: Simulation of sun-tracking error. | 18 |
| Figure 3.5: Tilting a single quadrant with respect to x-axis and y-axis. | 19 |
| Figure 3.6: Tilting two adjacent quadrant with respect to x-axis. | 19 |
| Figure 3.7: Tilting two diagonal quadrant with respect to x-axis and y-axis. | 20 |
| Figure 3.8: Flowchart of the procedure. | 21 |
| Figure 4.1: Irradiance map and cross-sectional profile on receiver plan at 1200 mm focal distance. | 22 |
| Figure 4.2: Spillage loss against the receiver plane dimension at 1200 mm focal distance. | 23 |
| Figure 4.3: Irradiance map and cross-sectional profile at the exit aperture of CCPC 1. | 24 |
| Figure 4.4: Irradiance map and cross-sectional profile at the exit aperture of CCPC 2. | 24 |
| Figure 4.5: Irradiance map and cross-sectional profile at the exit aperture of CCPC 3. | 25 |
| Figure 4.6: Irradiance map and cross-sectional profile at the exit aperture of CCPC 4. | 25 |

| | |
|---|----|
| Figure 4.7: Irradiance map and cross-sectional profile for 0° off-axis angle. | 27 |
| Figure 4.8: Irradiance map and cross-sectional profile for 0.2° off-axis angle. | 27 |
| Figure 4.9: Irradiance map and cross-sectional profile for 0.4° off-axis angle. | 28 |
| Figure 4.10: Irradiance map and cross-sectional profile for 0.6° off-axis angle. | 28 |
| Figure 4.11: Irradiance map and cross-sectional profile for 0.8° off-axis angle. | 28 |
| Figure 4.12: Irradiance map and cross-sectional profile for 1° off-axis angle. | 29 |
| Figure 4.13: The variation in solar flux distribution in percentage within the defined boundary area of 30 mm × 30 mm caused by the tracking error versus off-axis angles ($\Delta\theta$) from 0° to 1°. | 31 |
| Figure 4.14: Percentage of energy fallen into the defined receiver area of 60 mm × 60 mm with respect to perfect tracking against off-axis angle ranging from -1° to 1°. | 32 |
| Figure 4.15: Average SCR at exit aperture of all CCPC lens against focal distance. | 34 |
| Figure 4.16: Percentage of energy at the CCPC exit aperture compared with that at ideal focal distance against focal distance from 1150 mm to 1250 mm. | 35 |
| Figure 4.17: Irradiance map and cross-sectional profile for 0.2° tilting angle with respect to x-axis and y-axis. | 36 |
| Figure 4.18: Irradiance map and cross-sectional profile for 0.4° tilting angle with respect to x-axis and y-axis. | 37 |
| Figure 4.19: Irradiance map and cross-sectional profile for 0.6° tilting angle with respect to x-axis and y-axis. | 37 |
| Figure 4.20: Irradiance map and cross-sectional profile for 0.2° tilting angle with respect to x-axis. | 38 |
| Figure 4.21: Irradiance map and cross-sectional profile for 0.4° tilting angle with respect to x-axis. | 38 |

- Figure 4.22: Irradiance map and cross-sectional profile for 0.6° tilting angle with respect to x-axis. 39
- Figure 4.23: Irradiance map and cross-sectional profile for 0.2° tilting angle with respect to x-axis and y-axis. 40
- Figure 4.24: Irradiance map and cross-sectional profile for 0.4° tilting angle with respect to x-axis and y-axis. 40
- Figure 4.25: Average SCR on the receiver for the 3 cases against the tilting angle of the NIDC quadrant. 41
- Figure 4.26: Uniformly illuminated area on the receiver for the 3 cases against the tilting angle of the NIDC quadrant. 41
- Figure 4.27: Percentage of energy at the $60\text{ mm} \times 60\text{ mm}$ receiver with respect to no slope error against the tilting angle of NIDC quadrant. 42

LIST OF SYMBOLS / ABBREVIATIONS

| | |
|------------------|---|
| $A_{aperture}$ | aperture area, m ² |
| $A_{cell,des}$ | illuminated area of solar cell. m ² |
| BiPV | building integrated photovoltaic |
| CCPC | cross compound parabolic concentrator |
| C_{eff} | effective concentration ratio |
| C_{geo} | geometrical concentration |
| CPV | concentrator photovoltaic |
| C_{SOE} | effective concentration ratio of CCPC lens |
| CSP | concentrated solar power |
| DACPV | dense-array concentrator photovoltaic |
| DC | direct current |
| DNI | direct normal irradiance, W/m ² |
| f | focal distance, m |
| I_{sc}^1 | short-circuit current under 1-sun condition |
| I_{sc} | short-circuit current |
| J_{sc} | short-circuit current density |
| k | Boltzmann's constant, m ² kg s ⁻² K ⁻¹ |
| LCOE | levelised cost of electricity |
| MJSC | multi-junction solar cell |
| n | diode ideality factor |
| NIDC | non-imaging dish concentrator |
| $P_{aperture}$ | solar power transferred to cell area, W |
| PCE | power conversion efficiency |
| $P_{flux, cell}$ | incident solar power on the optics aperture, W |
| POE | primary optical element |
| PV | photovoltaic |
| q | electric charge, C |
| SCR | solar concentration ratio |
| SOE | secondary optical element |
| T | absolute temperature, K |
| T_o | operating temperature of solar cell, K |
| UHCPV | ultra-high concentrator photovoltaic |

| | |
|--------------|--|
| V_{OC}^1 | open-circuit voltage under 1-sun condition |
| V_{OC} | open-circuit voltage |
| α | acceptance angle, ° |
| η_{opt} | optical efficiency |
| θ | half opening angle, ° |

CHAPTER 1

INTRODUCTION

1.1 General Introduction

The world population is projected to increase by 2 billion people from 7.7 billion in the year 2019 to 9.7 billion in the year 2050 (United Nations, 2019). This growth in population is naturally followed by a rising energy consumption that is estimated to increase by 50% between 2018 and 2050. As such, to accommodate the increasing demand, electricity generation will rise by 79% in the same period. The generation of electricity is partially fuelled by the fastest growing energy source in this period – renewables, which includes solar, wind and hydroelectric power, whose consumption is estimated to grow by 3.1% per annum (Energy Information Administration, 2019).

According to the “Renewables 2019 Global Status Report” by REN21 (2019), in the year 2018, the annual global market for solar photovoltaics (PV) experienced a slight increase, surpassing the 100 GW level for the first time (including on-grid and off-grid capacity). In 2018, an estimated 2.4% of global electricity generation per annum, i.e. approximately 640 TWh of electricity per year worldwide was attributed to solar PV. However, despite improvements in adoption of renewables, energy efficiency and energy accessibility, the objectives of the Paris Agreement or of Sustainable Development Goal 7 are yet to be met. Due to increased fossil fuel consumption, global energy-related carbon dioxide emissions increased around 1.7% in 2018. Hence, in order that solar PV may serve as a primary source of electricity worldwide, challenges such as policy and regulatory uncertainty, financial and bankability difficulties as well as the integration of solar PV into electricity markets and systems in a reasonable and sustainable way have to be resolved.

Among the myriad solar PV technologies that aim to capture and convert solar energy into useful electrical or thermal energy, flat PV dominates the majority of the market share and is commonly installed solar power plant and building integrated photovoltaic (BiPV) system. This is because flat PV has a competitive production cost, comparatively low maintenance cost and is easy to install. However, the power conversion efficiency (PCE) of flat PV has flattened

out at 25% and it makes inefficient use of land area (Chong et al, 2017). Therefore, concentrator photovoltaic (CPV) technology has been proposed as an alternative for the generation of electricity at utility-scale due to its high efficiency. The concept behind CPV is the utilisation of concentrating optics that are more efficient in terms of cost which drastically reduce the area of the solar cell, allowing the deployment of costly but highly efficient solar cells and possibly a competitive levelised cost of electricity (LCOE) when compared with Concentrated Solar Power (CSP) and conventional flat PV. A competitive LCOE can be achieved when CPV is installed in some sunny regions with high Direct Normal Irradiance (DNI). Nevertheless, the CPV industry struggles to compete with the falling price of flat PV, resulting in many companies exiting the market and hence it is becoming more difficult to raise the capital required to scale (Phillips et al., 2015). That being said, the highest efficiency attained by CPV module till date is 38.9% by utilising III-V multi-junction solar cell (MJSC) with four junctions while mini-modules have realised a record efficiency of 43.4% (Weisenharth, Anton and Bett, 2018). It is undeniable that CPV systems have already exceeded the efficiency that traditional flat PV technology is capable of producing with room of further improvement in the future. This high efficiency introduces the possibility of significant reductions in systems costs, which allows CPV to remain competitive in the market.

Wong et al. (2017) proposed a design of ultra-high concentrator photovoltaic (UHCPV) system which uses non-imaging dish concentrator (NIDC) as its primary optical element and crossed compound parabolic concentrator (CCPC) as its secondary optical element. The UHCPV is capable of attaining effective ultra-high solar concentration ratio (SCR) of 1475 suns with a DC system efficiency of 31.8%. In this project, the proposed UHCPV is modelled in TracePro to be simulated by tracing sun rays. The optical characteristics of the UHCPV system including the flux distribution uniformity, spillage loss, SCR, tolerance angle against sun-tracking error, tolerance length against focal distance deviation and tolerance angle against slope error of the NIDC quadrant are simulated and analysed. Then, the results of TracePro are compared to the results obtained via ray-tracing numerical simulation technique done by Wong et al. (2017).

1.2 Importance of the Study

In developing an UHCPV power generation system, the role of solar concentration cannot be understated as the system converts solar energy which is highly focused into useful electrical energy. In the UHCPV system investigated in this paper, the primary concentrator is made of 480 facet mirrors forming the NIDC module to concentrate sunlight to a 2×2 array secondary CCPC fitted with MJSC at ultra-high SCR (> 1000 suns).

By using TracePro to model the UHCPV system, the flux distribution uniformity, solar concentration ratio and spillage loss at the $60 \text{ mm} \times 60 \text{ mm}$ receiver area can be determined. Furthermore, tolerance angle against sun-tracking error, tolerance length against focal distance deviation and tolerance angle against slope error of the NIDC quadrant can be simulated and analysed as well. This provides a cost-effective way of analysing the optical performance of the system and the effects of sun-tracking error, focal distance deviation and slope error of a quadrant of the NIDC can be investigated.

1.3 Problem Statement

The main problem detected by Khor (2019) after experimenting with the actual UHCPV prototype is that the mirrors of the NIDC were misaligned. As such, not all the solar irradiance was able to be reflected to the receiver. In fact, the area of the reflected light ray from the primary concentrator to the secondary concentrator ($16 \text{ cm} \times 11 \text{ cm}$) was larger than the area of the receiver ($6 \text{ cm} \times 6 \text{ cm}$). A huge amount of optical loss was incurred at the primary concentrator resulting in a SCR of 350 instead of the theoretical 1000 suns.

Also, the optical performance of the UHCPV system had not been simulated using TracePro. As such, important optical characteristics such as the flux distribution uniformity, spillage loss, SCR, tolerance angle against sun-tracking error, tolerance length against focal distance deviation and tolerance angle against slope error of the NIDC quadrant were not properly studied.

1.4 Aim and Objectives

The aim of the project is to investigate the optical characteristics of the UHCPV system using NIDC and CCPC via TracePro simulation.

- To model the UHCPV using TracePro and carry out ray-tracing simulation.
- To investigate the optical properties of the UHCPV system - flux distribution uniformity, spillage loss, SCR, tolerance angle against sun-tracking error, tolerance length against focal distance deviation and tolerance angle against slope error of the NIDC quadrant.

1.5 Scope and Limitation of the Study

The scope of this project is to evaluate the optical characteristics of the UHCPV system including the flux distribution uniformity, spillage loss, SCR, tolerance angle against sun-tracking error, tolerance length against focal distance deviation and tolerance angle against slope error of the NIDC quadrant.

The main problem encountered is that the effects of slope error on individual facet mirrors of the NIDC cannot be properly investigated. This is because to simulate the slope error of individual mirrors, their coordinates would have to be calculated and drawn separately in SolidWorks before being imported to TracePro for simulation. Also, the computing power of the device used for TracePro simulation limits the resolution of the irradiance map that can be obtained. For example, the computer used for this study can only simulate up to 10,000 rays as simulating more rays would result in the software not responding due to insufficient memory and computing power.

1.6 Contribution of the Study

This study has managed to model the UHCPV system using Tracepro to simulate the flux distribution uniformity, solar concentration ratio and spillage loss at the $60\text{ mm} \times 60\text{ mm}$ receiver area. Also, the SCR of the system is determined to be 2367.85 suns which is then compared to the 1475 suns obtained by Wong et al. (2017) using numerical ray-tracing technique. In addition, the tolerance angle against sun-tracking error, tolerance length against focal distance deviation and tolerance angle against slope error of the NIDC quadrant are investigated and their impact against the distribution of solar flux at the receiver is analysed. All these optical characteristics of the UHCPV system serve as a useful reference for future design of CPV systems in general and for optimising the existing UHCPV prototype in particular.

1.7 Outline of the Report

In the following section, literature review would be carried out on the various technologies and developments of CPV systems. Subsequently, the methodology for carrying the study is presented. Then the collected results are demonstrated and discussed. The conclusion will sum up the findings and give recommendations for future studies to be carried out.

CHAPTER 2

LITERATURE REVIEW

2.1 Introduction

In this section, a review on the development of concentrator photovoltaic (CPV) technology, each component of a CPV system and its developmental trend are discussed after researching various sources of journals, textbooks, articles and literature. Moreover, the work done by Wong et al. (2017) and Chong et al. (2017) which serve as a basis for this project would also be summarised and correlated to the current UHCPV prototype. Also, the effects of non-uniform illumination and increase in temperature on a CPV are reported in this section.

2.2 Literature Review

2.2.1 Overview of Concentrator Photovoltaic (CPV)

Concentrator photovoltaic (CPV) is one of the PV technologies which convert solar energy into useful electrical energy. The uniqueness of CPV compared to traditional PV is that it focuses the solar energy collected from a large optics area to a small solar cell. Solar concentration ratio (SCR) is defined as the optics area to the solar cell area ratio and has a dimensionless unit referred to as “suns or x ”. CPV can be divided into three classes: low concentration photovoltaic system (LCPV) with $1x < SCR < 30x$ using silicon solar cells, high concentration photovoltaic (HCPV) system with $SCR > 300x$ using high efficiency multi-junction solar cell (MJSC) as well as ultra-high concentration photovoltaic (UHCPV) system with $SCR > 1000x$.

As CPV is able to focus sunlight into a much smaller solar cell area compared to traditional flat PV, solar cells which are highly efficient and expensive can be adopted into its design. Though using much smaller and more efficient cells decreases the cost, CPV systems are generally more complex compared to conventional PV systems. The point is to develop a CPV system whose savings in semiconductor area and superior efficiency is sufficient to compensate the cost incurred due to its design complexity. In this way, CPV can compete with traditional PV systems in the market (Algora and Rey-Stolle, 2016).

The pros and cons of CPV are summarised in Table 2.1 below:

Table 2.1: The pros and cons of CPV (Philipps et al., 2015, p. 9).

| CPV Pros | CPV Cons |
|--|--|
| High efficiencies for DNI | HCPV cannot use diffuse radiation while LCPV can only use diffuse radiation partially |
| Low temperature coefficients | High accuracy and reliability is needed for tracking |
| No cooling water is needed for passively cooled systems | Frequent cleaning is needed to reduce soiling losses |
| Additional use of waste heat possible for systems with active cooling | Smaller market as only regions with high DNI is suitable for installation and it cannot be easily set up on rooftops |
| Modular – kW to GW scale | Competing technologies for electricity production have high decrease in cost |
| High and consistent energy production throughout the day by utilising sun-tracking | Low bankability and market awareness due to shorter track record compared to flat PV |
| Very low energy payback time | Emerging technology, thus without a history of production and higher risk |
| Potential additional use of land | Extra optical losses |
| Prospects for cost-effective local manufacturing in certain stages | Insufficient standardisation of technology |
| Lower sensitivity to fluctuations in semiconductor prices | |
| More potential for increase in efficiency in the future compared to single-junction flat plate systems | |

Besides, conventional flat PV panel has a power conversion efficiency (PCE) that is saturated at 25%. On the other hand, as of 2018, the highest CPV module efficiency using solar cells based on four-junction III-V is recorded at 38.9% while an efficiency of 43.4% has been attained by mini-modules (Weisenharth, Anton and Bett, 2018). In addition, CPV and CPV/T has the potential of delivering an overall efficiency of 60% based on the findings reviewed by George et al. (2018).

Nevertheless, according to the report produced by Philipps et al. (2015), many companies that produce CPV have closed, bankrupted, turned their focus away from CPV to conventional PV or been absorbed by larger corporations since 2011. The major reason behind this development is that CPV struggles to compete in terms of cost with traditional flat c-Si PV modules. The manufacturers expect CPV to compete with flat PV on LCOE basis but the scalability of CPV remains a challenge.

Based on an industry survey and literature done by Philipps et al. (2015), CPV system prices (including installation for 10 MW CPV power plants) range between €1400/kWp and €2200/kWp. Moreover, CPV power plants have a estimated LCOE between €0.10/kWh to €0.15/kWh at places with a DNI of 2000 kWh/(m²a) and €0.08/kWh to €0.12/kWh at places with a DNI of 2500 kWh/(m²a). The report also shows that CPV can potentially reduce LCOE. If the growth of installations is sustained through 2030, CPV is estimated to have a cost lying between €0.045/kWh and €0.075/kWh and the corresponding system prices would drop to the range between €700 and €1100/kWp.

CPV technology shows extraordinary potential for further improvements in efficiency, which helps to drive down LCOE and thus making it competitive in the market. As CPV is a relatively new technology, more R&D must be done to improve its performance.

2.2.2 Components in CPV and Specific Design Requirements

2.2.2.1 Concentrator Optics

As discussed by Weisenharth, Anton and Bett (2018), one of the most significant figure of merit for an optical element is its optical efficiency which measures the ratio of the incident solar power on the aperture of the optics that is transferred to the cell area.

$$\eta_{opt} = \frac{P_{flux,cell}}{P_{aperture}} \quad (2.1)$$

The optical loss of a Fresnel lens can be attributed to transmission losses, geometric losses, dispersion losses, reflection losses and shading caused by the heat distributor and solar cell. These optical losses are to be taken into account when designing the optical component of the CPV.

Moreover, the focal distance, f plays an important role as it defines the module height and affects the half opening angle, θ as the angle to the optical axis at which most of the rays can reach the solar cell. Besides, the geometrical concentration, C_{geo} is another important design consideration which is defined in Equation 2.2 below and illustrated in Figure 2.1.

$$C_{geo} = \frac{A_{aperture}}{A_{cell,des}} \quad (2.2)$$

where

$$A_{aperture} = \text{Aperture area}$$

$$A_{cell,des} = \text{Illuminated area of the solar cell}$$

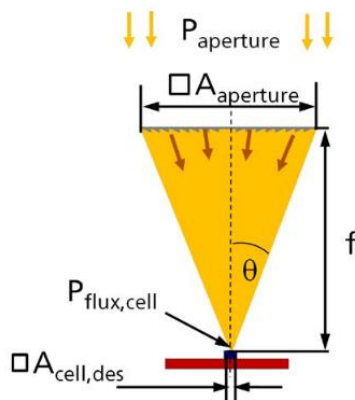


Figure 2.1: Defining focal distance, f , half opening angle, θ and indicating the input position of solar power, $P_{aperture}$ and $P_{flux,cell}$.

Furthermore, the acceptance angle, α is another important aspect of a CPV module. Concentration acceptance product (CAP) can be used to relate both C_{geo} and α in Equation 2.3 below.

$$CAP = \sqrt{C_{geo}} \sin \alpha \quad (2.3)$$

In addition, imaging and non-imaging optics are two separate classifications of concentrator optics. Imaging point focus optics projects a miniaturised image of the light source upon the area of the solar cell, e.g. aspheric plano-convex lens designs which includes paraboloidal mirrors or Fresnel lenses. On the other hand, non-imaging or anidolic optics focus on the optimal power transfer and the image of the source is not formed. Hence, multiple forms of the source with different target flux distribution can be designed (Weisenharth, Anton and Bett, 2018).

2.2.2.2 Primary concentrator optics (POE)

POE can be made of reflective mirrors with no chromatic aberration and have high optical efficiencies. Large parabolic mirrors and heliostats can be built based on reflective optics in CPV systems.

On the other hand, CPV often adopt primary lens optics that are made of multiple lenses with the areas of single unit ranging from 4 cm² to 1000 cm² that are arranged in the form of an array. This allows for parallel manufacturing which lowers the costs but there are still difficulties in manufacturing large areas and arrays cost-effectively. Hence, to reduce material and weight, Fresnel lens structures are invented. Nevertheless, the use of primary lens optics will introduce loss due to chromatic aberration as a result of the dependency of wavelength on the refractive index (Weisenharth, Anton and Bett, 2018).

2.2.2.3 Secondary concentrator optics (SOE)

SOE are installed in CPV to increase concentration, acceptance angle or to homogenise the distribution of the flux. SOE has effective concentration ranging between 300x and 1100x but can be reach magnitudes at multiples of the average value. An important point to take note when designing SOE is the coupling between the SOE and the cell as it influences the performance and the

reliability of the CPV system in the long term. Furthermore, SOE also increase angular tolerance, decrease electrical losses in the cell and increase fill factor (FF) by making the flux more uniform, reducing losses produced by the chromatic effect of refractive POE and reducing cell architecture and design sensitivity to focal distance and thus to the changes in surrounding temperature.

There are several designs available for SOE including reflective SOE, solid SOE with refractive index higher than air, refractive compound parabolic concentrators (CPCs) or kaleidoscope-shaped SOE which are invented to homogenise the distribution of the flux and to increase the CAP (Weisenharth, Anton and Bett, 2018).

2.2.2.4 Multi-Junction Solar Cell (MJSC)

A single MJSC is made of 20 to 50 distinct layers that can be designed by using a multitude of materials with different bandgaps and different methods. A doped substrate like germanium (Ge), silicon (Si), indium phosphide (InP), gallium antimonide (GaSb) or gallium arsenide (GaAs) is normally used to grow a III-V-based MJSC. Shown in Figure 2.2 below are a summary of the technologies, methods and materials used to design III-V MJSC (Weisenharth, Anton and Bett, 2018).

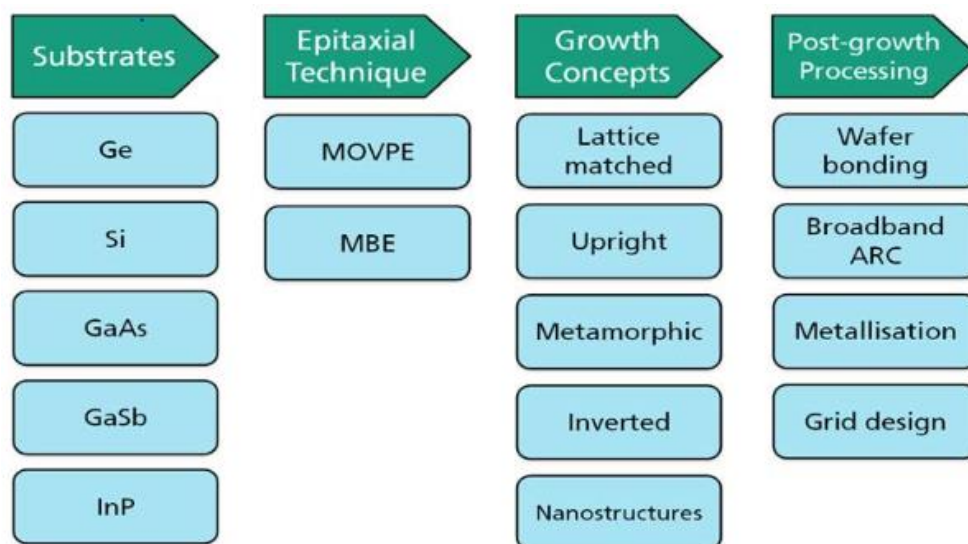


Figure 2.2: Summary of the technologies, methods and materials used to design III-V MJSC.

2.2.3 Developmental Trends in CPV Technology

In order that HCPV can be more competitive in cost on the LCOE level, a higher efficiency is desired. In Figure 2.3 below, the increase in efficiency since 2000 is shown and the estimations of the European Photovoltaic Technology Platform in 2011 are used to plot the trend lines (Philipps et al., 2015).

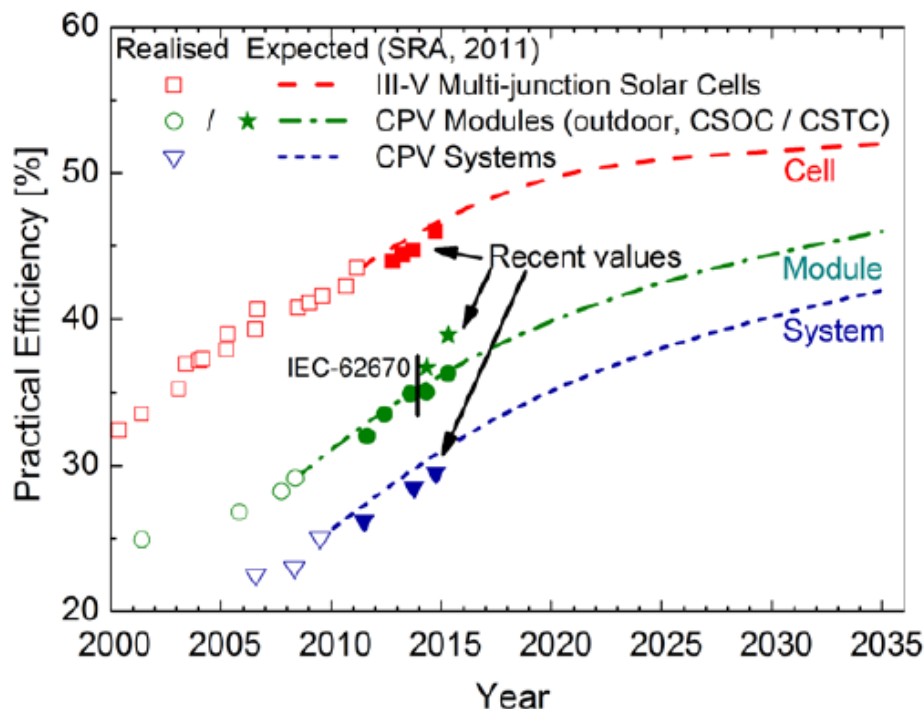


Figure 2.3: Development of efficiencies of III-V multi-junction solar cells and CPV modules.

To decrease the LCOE of the energy produced by HCPV technology, one of the key improvements that can be made is by increasing the efficiency of III-V MJSC. Since 2002, an annual 0.9 % increase in efficiency is achieved and the solar cells made by Sharp and Fraunhofer ISE have reached unprecedented efficiencies of 44.4 % and 46.0 % for triple- and four-junction solar cells, respectively (Philipps et al., 2015). Various cell architectures which use different combinations of materials are being explored by researchers in hope of raising the efficiency of the MJSC.

2.2.4 Work Done by Wong et al. (2017) and Chong et al. (2017)

The research done by Wong et al. (2017) and Chong et al. (2017) are of particular interest to this project as the UHCPV used in this project are designed based on their works.

Wong et al. (2017) has presented a methodical approach for optimising the design of ultra-high concentrator photovoltaic (UHCPV) system which uses non-imaging dish concentrator (NIDC) as its POE and crossed compound parabolic concentrator (CCPC) as its SOE. In the process of designing POE and SOE, the focal distance, rim angle and spillage losses of the dish concentrator are considered. Besides, to avoid overestimation of output power, the imperfection factors, i.e. mirror reflectivity of 93%, circumsolar ratio of 0.2, lens' optical efficiency of 85% and mirror surface slope error of 2 mrad were considered in the simulation. The paper propose an UHCPV system that is capable of attaining effective ultra-high SCR of 1475 suns with a DC system efficiency of 31.8%.

On the other hand, Chong et al. managed to construct a prototype of dense array concentrator photovoltaic (DACPV) system comprising of NIDC and CCPC coupled to MJSC. At DNI ranging from 740 to 801 W/m², the system efficiency of the prototype was measured between 16.1% and 17.4%.

2.2.5 Effect of Non-Uniform Illumination on the Performance of CPV

According to Li et al. (2018), there are two different categorisations of the non-uniform illumination: a single solar cell with the non-uniform illumination or series-connected cells with dissimilar illumination on each cell surface. As solar cells are normally connected in series, if each cell cannot maintain exactly the same performance, current mismatch would occur during which the total power output is smaller than the total of individual power.

A few factors may lead to non-uniform illumination, e.g. improper design of concentrator optics, unsuitable materials being used, profile errors and manufacturing defects. Moreover, inappropriate tracking system, deviation in the position of optics and cell, shading and spectral response could also lead to non-uniform illumination.

Non-uniform illumination can lead to a significant drop in open-circuit voltage, efficiency and fill factor particularly for MJSC. That being said, the

problem can be alleviated by altering the cell surface pattern as well as selecting proper cell material and concentrator.

2.2.6 Effect of Temperature on the Performance of CPV

Temperature will influence the performance, operation, and reliability of CPV systems at all levels. In the field, temperature varies as solar irradiation, humidity and wind fluctuates. The negative impact of temperature variation on the energy output of the system must be minimised.

Algora and Rey-Stolle (2016) explains that temperature affects the performance of the solar cell, which is a semiconductor device. The bandgap of most of the semiconductor materials reduces as temperature rises. Consequently, this leads to a fluctuation in short-circuit current density, J_{SC} in the MJSC. This is because in the MJSC the J_{SC} each sub-cell depends on its bandgap and on the bandgaps of the sub-cells on top.

Also, the temperature coefficient of the V_{OC} is always negative, i.e. the higher the temperature, the lower the V_{OC} . It should also be noted that the temperature coefficient of the V_{OC} is directly related to the actual V_{OC} of the cell for a given temperature and bandgap, i.e. the higher the V_{OC} , the lower its temperature coefficient. As such, for the same material, solar cells with higher quality have lower sensitivity against temperature.

2.3 Summary

CPV is an emerging PV technology characterised by its use of optical concentrators to concentrate sunlight into a small area of high-efficiency, expensive multi-junction solar cell. Based on the literature review done, it is clear that though CPV at the current stage still has a higher production cost than traditional flat PV, it has enormous potential in increasing efficiency and thus lowering LCOE. As such, CPV is an important field of research and is essential in transforming the world from a fossil-fuel-based society into a society powered by environmentally-friendly and sustainable solar energy.

CHAPTER 3

METHODOLOGY AND WORK PLAN

3.1 Introduction

In this section, the UHCPV system is modelled in TracePro to be simulated by tracing sun rays.

The optical properties of the UHCPV system including the flux distribution uniformity, spillage loss, SCR, tolerance angle against sun-tracking error, tolerance length against focal distance deviation and tolerance angle against slope error of the NIDC quadrant are simulated and analysed.

In addition, the results of TracePro are compared to the results obtained via the ray-tracing numerical simulation technique done by Wong et al. (2017).

3.2 System description

The schematic diagram of the UHCPV system is shown in Figure 3.1 below. The NIDC (POE) has a width (D) of about 1000 mm designed to focus sunlight onto the CCPC lenses (SOE) at a focal distance (F) of 1200 mm along the Z -axis. The NIDC consists of 480 flat facet mirrors each with a dimension of $40\text{ mm} \times 40\text{ mm}$ arranged into 22×22 columns. Four mirrors in the central region of the NIDC are removed to avoid shading by the receiver. To prevent shadowing and blocking among the neighbouring mirrors, the facet mirrors are gradually lifted from the central to the peripheral regions of the NIDC. Also, a gap of 5 mm is designed between the facet mirrors to provide tolerance for manufacturing defects during installation. The detailed design of the NIDC is described by Tan, Chong and Wong (2014).

On the other hand, B270 Schott glass CCPC lens is used as the SOE to homogenize the non-uniform illumination distributed on the receiver plane and to focus the sunlight concentrated by the NIDC onto MJSC. The CCPC is arranged in 2×2 arrays with each lens having a square entrance aperture of $2a = 24\text{ mm}$ and an exit aperture of $2a' = 9.8\text{ mm}$ after considering the dimension of the MJSC. The CCPC lens has refractive index (n) of 1.5-1.56, half acceptance angle of CCPC, $\theta_i = 37.77^\circ$, length of CCPC lens, $L =$

37.88 mm and geometrical concentration ratio of CCPC lens, $C_{geo} = 5.998$.

The cross-sectional view of the CCPC lens is shown in Figure 3.2 below.

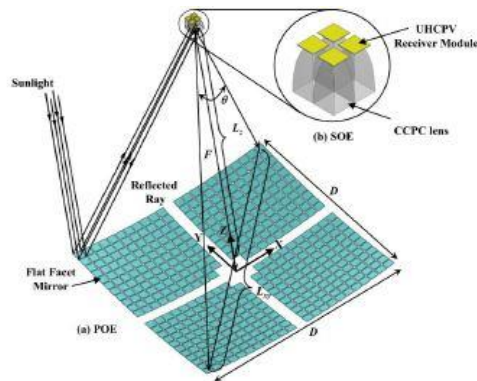


Figure 3.1: Schematic diagram of UHCPV system.

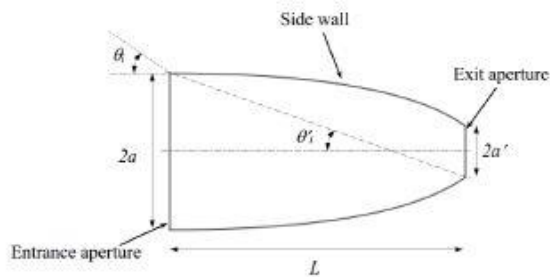


Figure 3.2: Cross-sectional view of CCPC lens.

After taking into account of the various components of the UHCPV system, the system is modelled in Solidworks and then imported to TracePro to be simulated as shown in Figure 3.3 below.

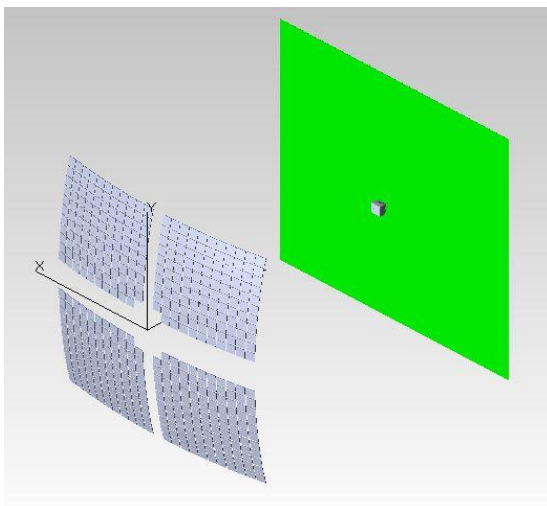


Figure 3.3: TracePro modelling of the UHCPV system.

3.3 Ray tracing simulation

TracePro is used to model and simulate the UHCPV system. During the simulation, the incident solar irradiance is assumed to be 1000 W/m^2 (1 sun) onto the NIDC. All the facet mirrors are set to have reflectance of 94.87%. To produce an irradiance map with decent resolution, each simulation is done by tracing 10,000 rays. Moreover, solar disc effect is simulated by defining surface source property as “solar” for both spectral and rectangular types.

3.3.1 SCR on the receiver area at 1200 mm focal distance

By assuming a fixed receiver area of $60 \text{ mm} \times 60 \text{ mm}$ and a fixed width of the NIDC, $W = 1000 \text{ mm}$, the solar flux distribution on the receiver at focal distance, $F = 1200 \text{ mm}$ is simulated and analysed. The maximum and average SCRs on the receiver are recorded and the irradiance map as well as cross-sectional profile is shown.

3.3.2 Spillage loss

Spillage loss is defined as the percentage of sun ray falling beyond the receiver area. The square receiver plane is set at 1200 mm focal distance and its dimension is varied from $1 \text{ mm} \times 1 \text{ mm}$ to $7 \text{ mm} \times 7 \text{ mm}$ with 1 mm increment. The graph of spillage loss against receiver dimension is plotted and the optimum dimension of the receiver is determined.

3.3.3 Comparison with the results of Wong et al. (2017)

The maximum and average SCR on the receiver area, spillage loss, optimum receiver dimension and the final SCR on the MJSC simulated using TracePro are compared to similar work done via numerical simulation by Wong et al. (2017).

3.3.4 System performance with sun-tracking error

The effect of off-axis aberration on the solar flux distribution caused by the sun-tracking error is simulated by changing the off-axis angles $\Delta\theta$ from 0° to 1° . The the rotation of the light source in TracePro is rotated about x-axis from 0° to 1° as shown in Figure 3.4 below. The tolerance angle of the UHCPV with at least 95% energy compared to perfect tracking condition is calculated.

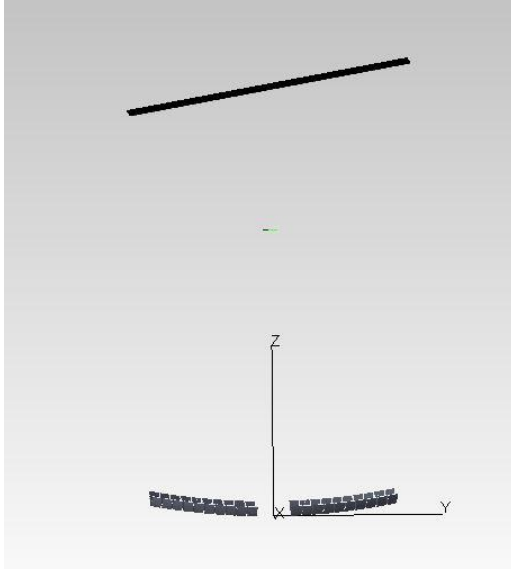


Figure 3.4: Simulation of sun-tracking error.

3.3.5 System performance with focal distance deviation

The NIDC was designed to focus sunlight on a $60\text{ mm} \times 60\text{ mm}$ receiver at a focal distance of 1200 mm. However, during the installation of the receiver minute error may occur and reduces the performance of the system. The effect of focal distance deviation on the distribution of solar flux is simulated by varying the focal distance, F from 1150 mm to 1250 mm. The average SCR at the exit apertures of the CCPC lens are recorded and the tolerance length with not more than 5% of energy loss compared to ideal 1200 mm focal distance is calculated.

3.3.6 System performance with slope error of NIDC quadrant

Slope error may occur during manufacturing process which results in non-uniform solar illumination on the receiver and reduced system performance. TracePro is used to simulate slope error of an entire quadrant of the NIDC and its effect on the solar flux distribution. 3 scenarios are simulated: a single quadrant is tilted with respect to x-axis and y-axis (Figure 3.5), two adjacent quadrants are tilted with respect to x-axis (Figure 3.6) and two diagonal quadrants are tilted with respect to x-axis and y-axis (Figure 3.7). The tolerance angle of the UHCPV with less than 5% loss of energy resulted by the slope error is calculated.

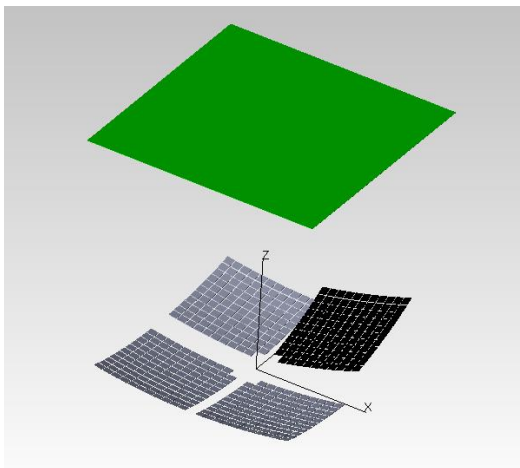


Figure 3.5: Tilting a single quadrant with respect to x-axis and y-axis.

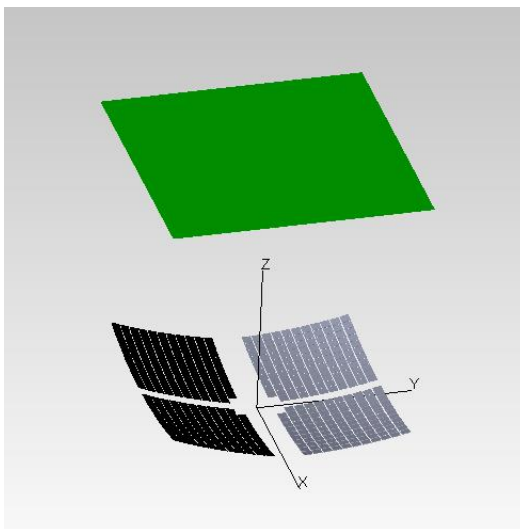


Figure 3.6: Tilting two adjacent quadrant with respect to x-axis.

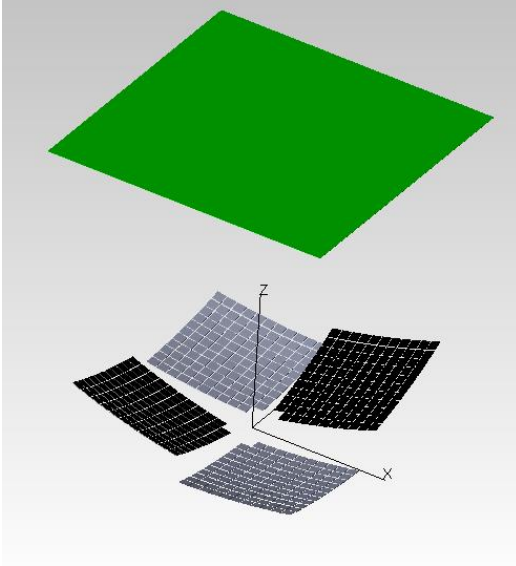


Figure 3.7: Tilting two diagonal quadrant with respect to x-axis and y-axis.

3.4 Summary

The UHCPV system is modelled in TracePro and ray-tracing simulation is carried out to determine its optical characteristics such as flux distribution uniformity, SCR, spillage loss, tolerance angle against sun-tracking error, tolerance length against focal distance deviation and tolerance angle against slope error of the NIDC quadrant. The results are compared to work done by Wong et al. (2017). The flowchart for carrying out the study is summarised in Figure 3.8 below.

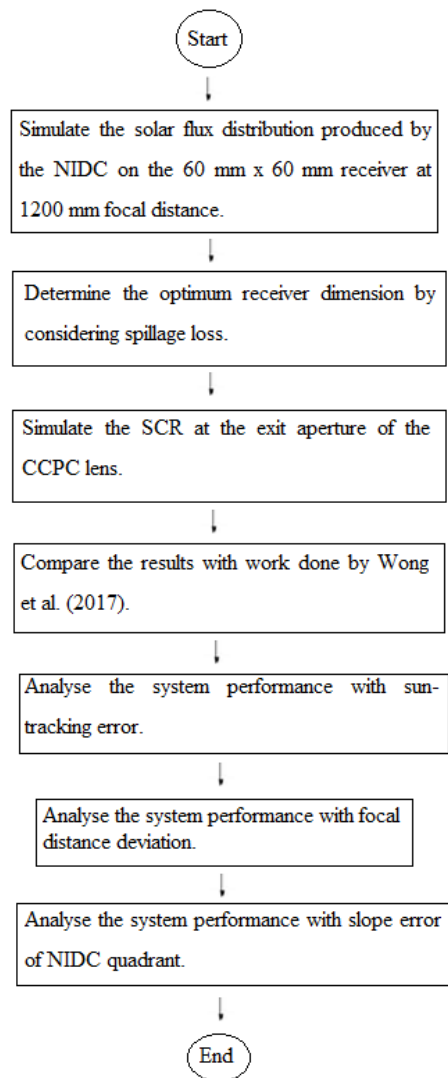


Figure 3.8: Flowchart of the procedure.

CHAPTER 4

RESULTS AND DISCUSSION

4.1 Introduction

In this section, the simulation results of flux distribution uniformity, SCR, spillage loss will be discussed and compared to work done by Wong et al. (2017). Moreover, the performance of the system with sun-tracking error, focal distance deviation and slope error of the NIDC quadrant are investigated and analysed.

4.2 SCR on the receiver area at 1200 mm focal distance

To simulate the distribution of solar flux, the receiver area is set as $60\text{ mm} \times 60\text{ mm}$ at 1200 mm focal distance. The resulting irradiance map and profile plot of the receiver area are shown in Figure 4.1 below.

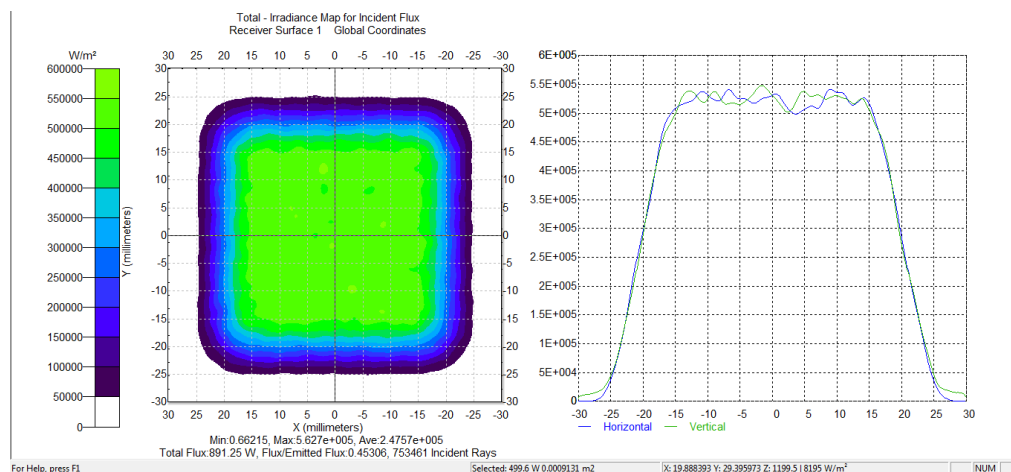


Figure 4.1: Irradiance map and cross-sectional profile on receiver plan at 1200 mm focal distance.

At 1200 mm focal distance, the uniformly illuminated area is about $30\text{ mm} \times 30\text{ mm}$ but this area has a SCR of around 525 suns. The average SCR on the entire receiver area is 247.57 suns. The solar energy inside the uniformly illuminated area is 52.5%.

4.3 Spillage loss

The dimension of the square receiver plane is varied from $1\text{ mm} \times 1\text{ mm}$ to $7\text{ mm} \times 7\text{ mm}$ with an increment of 1 mm to determine the spillage loss at a focal distance of 1200 mm. Figures 4.2 illustrates the spillage loss against the receiver plane dimension at 1200 mm focal distance.

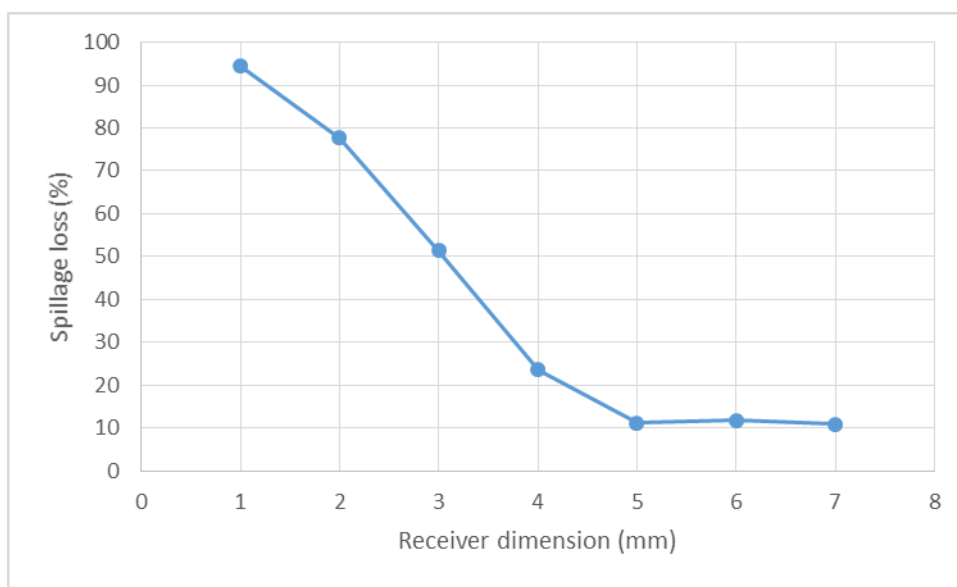


Figure 4.2: Spillage loss against the receiver plane dimension at 1200 mm focal distance.

From Figure 4.2, it is shown that at 1200 mm focal distance, the uniformly illuminated area is $3\text{ mm} \times 3\text{ mm}$. However, it is not advisable to design a receiver plane that only covers the uniformly illuminated area because the spillage loss is as high as 51.3%. In order to minimise the spillage loss and avoid the oversizing the receiver, the receiver plane dimension has to be selected properly. In this UHCPV system, the receiver plane with a dimension of $60\text{ mm} \times 60\text{ mm}$ should be chosen as it only has a spillage loss of 11.8%. Further increase of the receiver area can no longer achieve significant reduction in spillage loss.

4.4 SCR at exit aperture of CCPC

From the results discussed above, the at a focal distance of 1200 mm, the optimum receiver area is $60\text{ mm} \times 60\text{ mm}$. An array of 2×2 B270 Schott glass CCPC lens placed at a focal distance of 1200 mm to be used as the SOE. The resulting irradiance map and cross-sectional profile of the exit aperture of each of the CCPC lens are shown in Figure 4.3 to Figure 4.6 below.

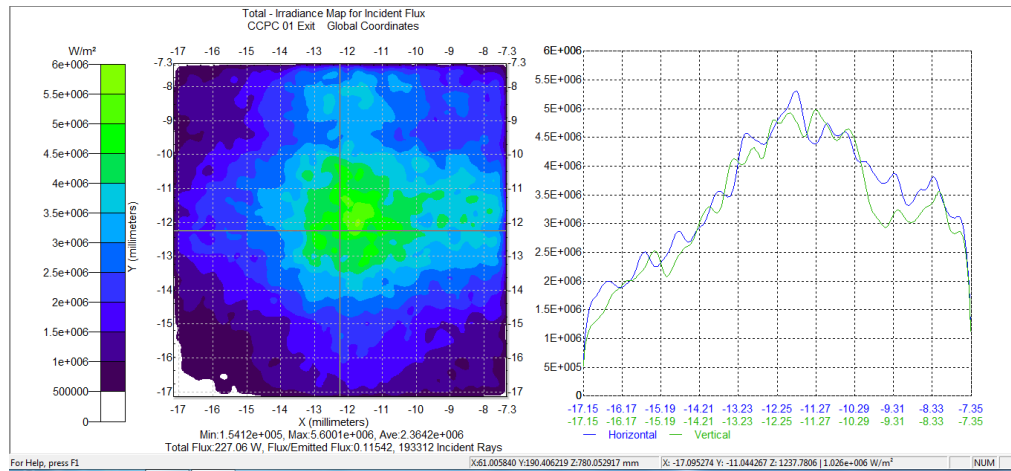


Figure 4.3: Irradiance map and cross-sectional profile at the exit aperture of CCPC 1.

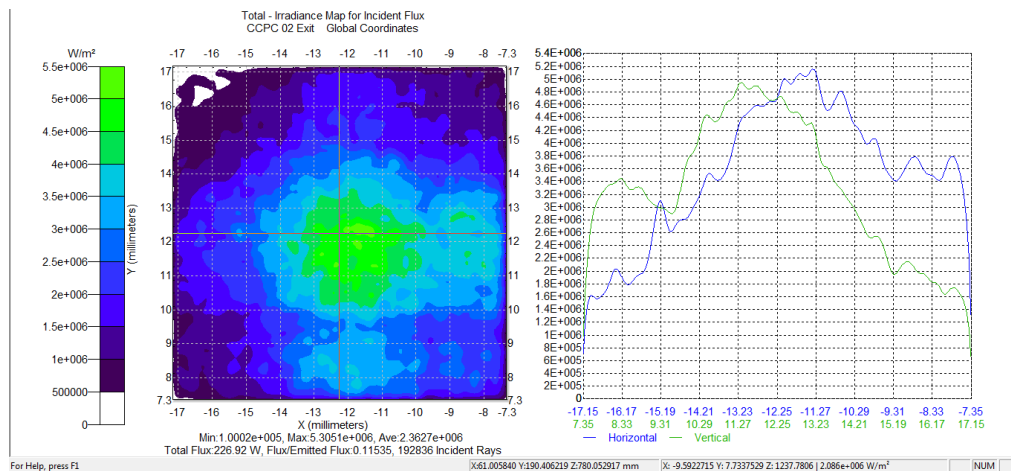


Figure 4.4: Irradiance map and cross-sectional profile at the exit aperture of CCPC 2.

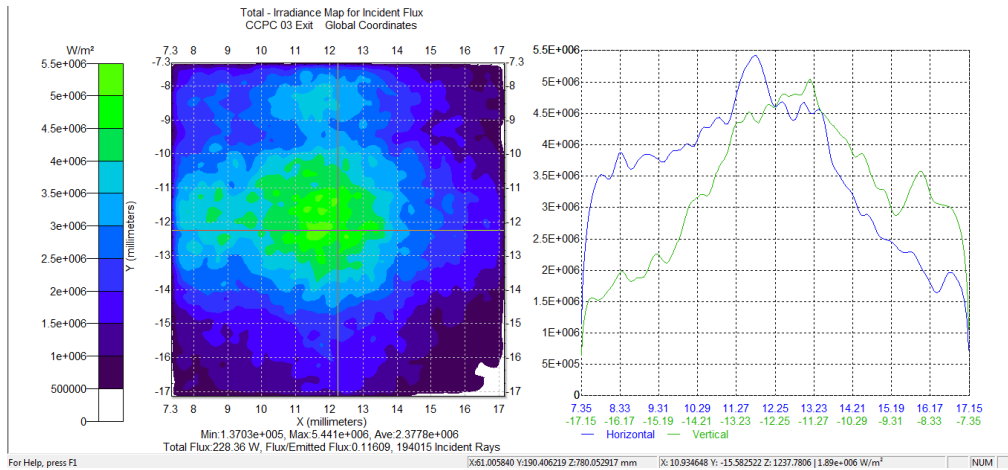


Figure 4.5: Irradiance map and cross-sectional profile at the exit aperture of CCPC 3.

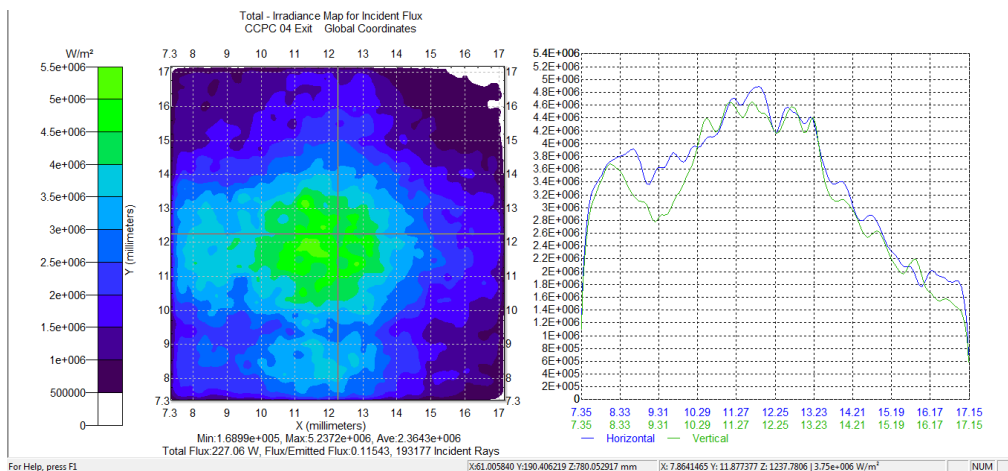


Figure 4.6: Irradiance map and cross-sectional profile at the exit aperture of CCPC 4.

From the figures above, the average SCR at the exit aperture is simulated as 2367.85 suns. This result is compared to the work done by Wong et al. (2017) below.

4.5 Comparison of results to work done by Wong et al. (2017)

In the work of Wong et al. (2017) titled “Design optimization of ultra-high concentrator photovoltaic system using two-stage non-imaging solar concentrator”, ray-tracing numerical simulation technique is used to study the optical characterisation of the UHCPV. Their work recommended an optimum F/D ratio of 1.4 at around 400 suns SCR and a receiver area of $6\text{ cm} \times 6\text{ cm}$ after considering the maximum SCR, spillage loss and the rim angles of the NIDC. The effective SCR, C_{eff} of the MJSC is calculated as 1475 suns using the following equation.

$$C_{eff} = C_{POE} \times C_{SOE}$$

By using TracePro, the UHCPV system with a focal distance of 1200 mm is modelled. The SCR at the uniformly illuminated area is found to be 525 suns. This result is reasonably close to the C_{POE} of 400 suns simulated by Wong et al. (2017) as the TracePro simulation only takes into account the circumsolar effect and not the slope error. Also, by considering the spillage loss, the receiver area is optimised to $60\text{ mm} \times 60\text{ mm}$ similar to that suggested by Wong et al. (2017).

The effective SCR, C_{eff} of the TracePro simulation has an average of 2367.85 suns. This result is close to the expected C_{eff} of 2441.25 suns which is the multiple of the C_{POE} of 525 suns obtained in TracePro and C_{SOE} of 4.65 suns as discussed in Lee et al. (2020) after taking into account of the optical losses. This C_{eff} is higher than the 1475 suns calculated by Wong et al. (2017) as the TracePro simulation does not take into account the effect of slope error on the NIDC and Wong et al. (2017) calculated the C_{SOE} to be 7.97.

4.6 System performance with sun-tracking error

Figure 4.7 to Figure 4.12 below illustrate solar flux distribution and cross-sectional profile within the receiver area of $60\text{ mm} \times 60\text{ mm}$ for off-axis angles of 0° , 0.2° , 0.4° , 0.6° , 0.8° and 1° while the focal distance is maintained at 1200 mm .

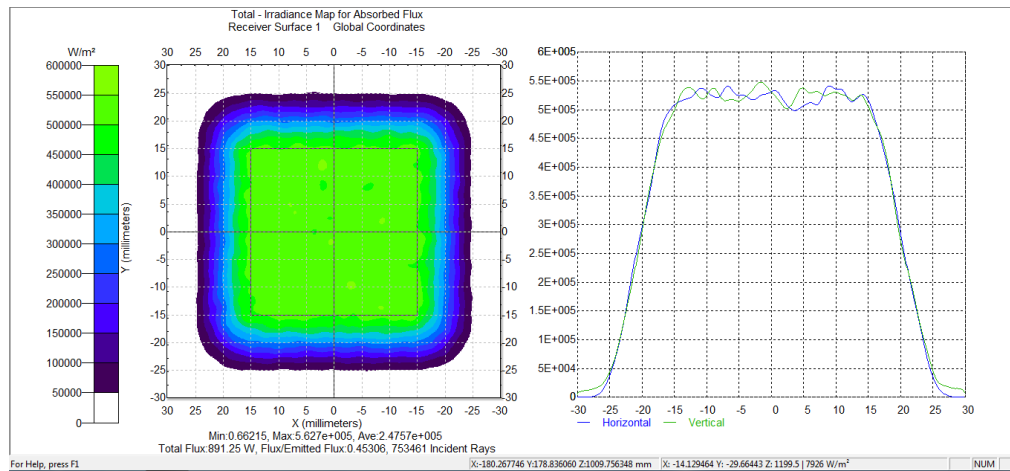


Figure 4.7: Irradiance map and cross-sectional profile for 0° off-axis angle.

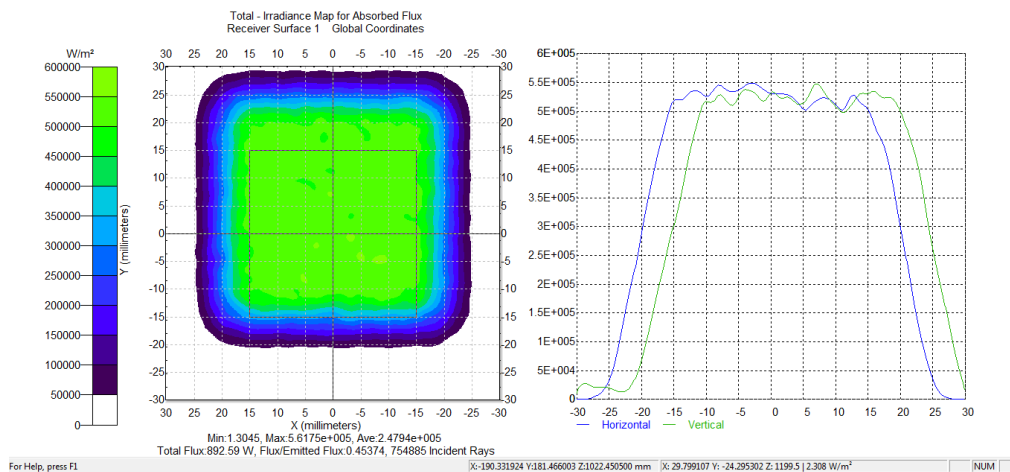


Figure 4.8: Irradiance map and cross-sectional profile for 0.2° off-axis angle.

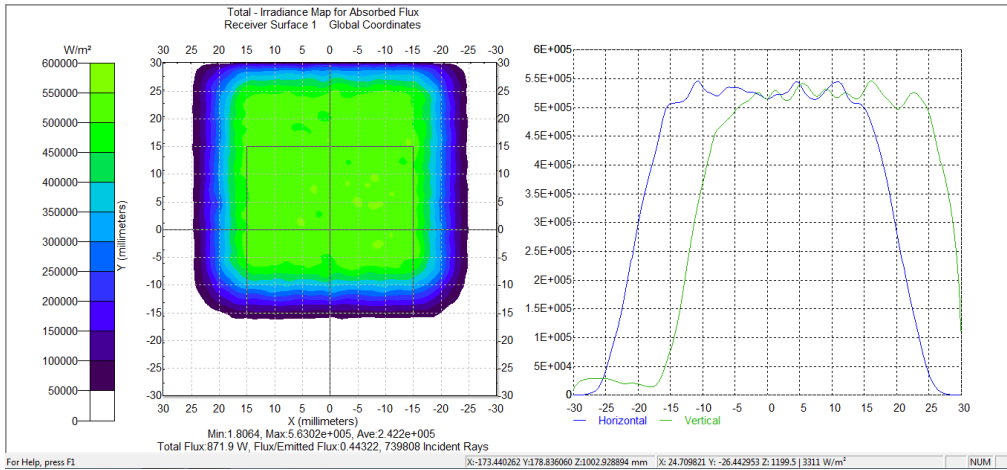


Figure 4.9: Irradiance map and cross-sectional profile for 0.4° off-axis angle.

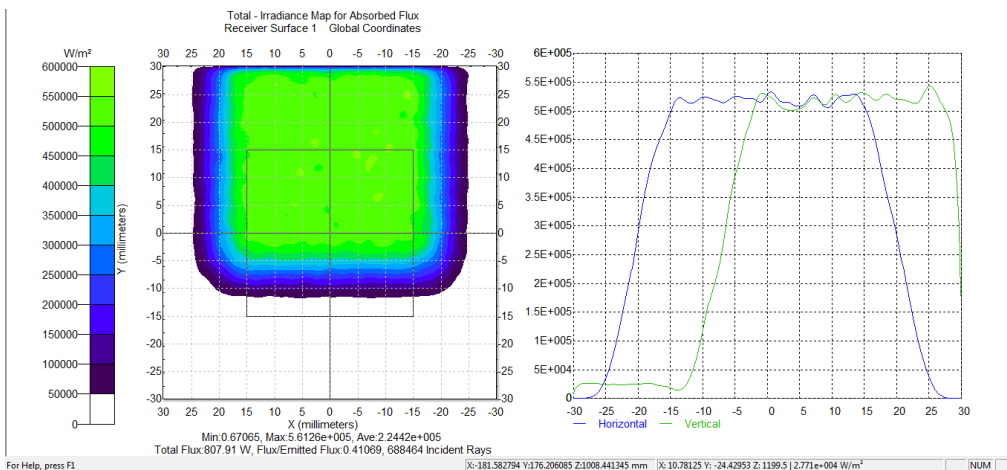


Figure 4.10: Irradiance map and cross-sectional profile for 0.6° off-axis angle.

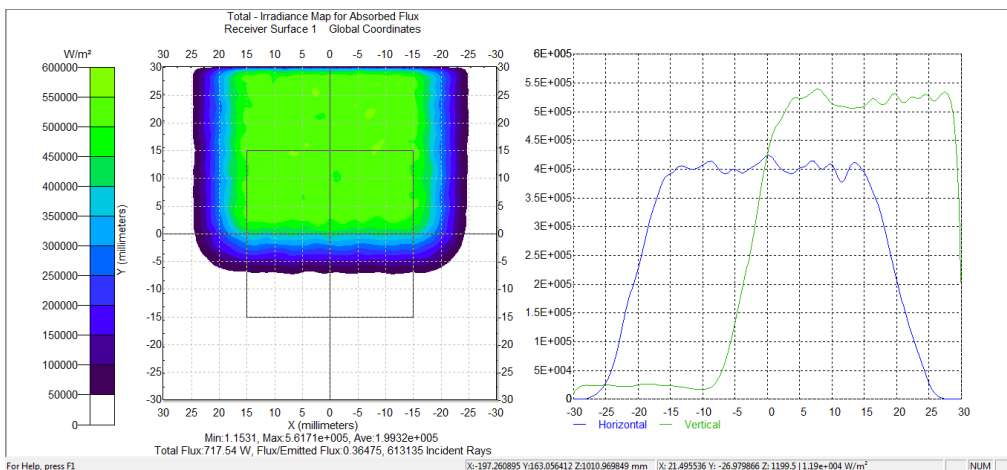


Figure 4.11: Irradiance map and cross-sectional profile for 0.8° off-axis angle.

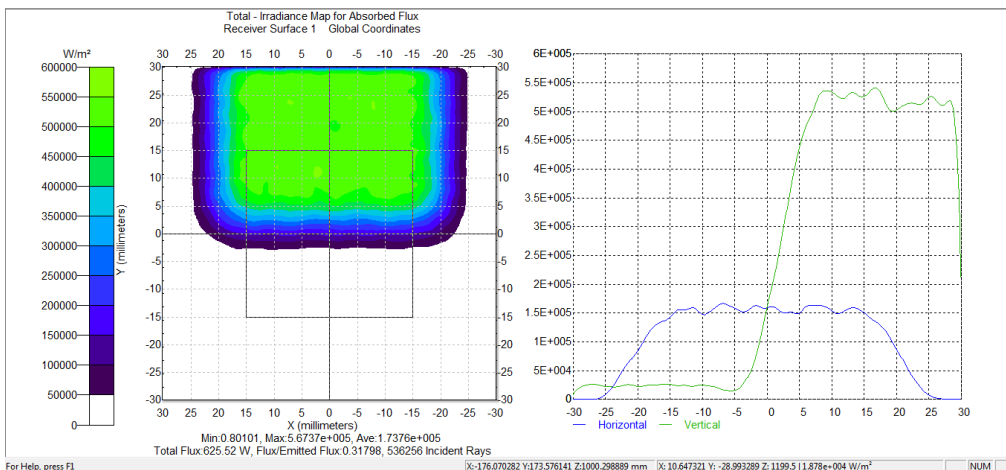


Figure 4.12: Irradiance map and cross-sectional profile for 1° off-axis angle.

Figure 4.7 shows that when there is no off-axis angle (0°), perfect sun-tracking condition is achieved and the facet mirrors are focuses the sunlight onto the receiver. Nevertheless, as the off-axis angle increases, the uniformly illuminated area moves away from centre of the receiver. From the cross-sectional profile along the x-axis, it can be seen that significant reduction in solar irradiance along the x-axis only occur at 0.8° and 1° off-axis angle. This is because after an off-axis angle of 0.8° and 1°, the uniformly illuminated area will shift beyond the receiver area.

Table 4.1 below records results obtained in Figure 15 to Figure 20 for different off-axis angles.

Table 4.1: Characteristics of solar irradiation for different off-axis angles including 0° , 0.2° , 0.4° , 0.6° , 0.8° and 1° with a focal distance of 1200 mm.

| Off-axis angle (degree) | Average SCR within receiver area of $60\text{ mm} \times 60\text{ mm}$ (suns) | Variation of flux distribution contained in the defined area of $30\text{ mm} \times 30\text{ mm}$ due to sun-tracking error (%) | Percentage of energy contained in the defined area of $30\text{ mm} \times 30\text{ mm}$ (%) |
|--------------------------------|---|--|--|
| 0 | 247.57 | 0 | 52.50 |
| 0.2 | 247.94 | 0.95 | 52.92 |
| 0.4 | 242.2 | 9.45 | 48.60 |
| 0.6 | 224.42 | 24.06 | 43.99 |
| 0.8 | 199.32 | 39.02 | 39.77 |
| 1 | 173.76 | 53.39 | 34.86 |

To analyse the effect of sun-tracking error on the distribution of solar flux, an $30\text{ mm} \times 30\text{ mm}$ border is defined at the centre of the receiver area which is also the size of the uniformly illuminated area when no sun-tracking error occurs. As the off-axis angle increases from 0° to 1° , uniformly illuminated area will move away from the defined border and the SCR at one end of the border will reduce. The variation in distribution of solar flux is calculated as the percentage difference in energy of the distribution of solar flux within the defined area of $30\text{ mm} \times 30\text{ mm}$ at a certain off-axis angle compared to that when no sun-tracking error occurs. In Figure 4.13 below, the graph of the variation in distribution of solar flux as a result of sun-tracking error against off-axis angle from 0° to 1° is plotted.

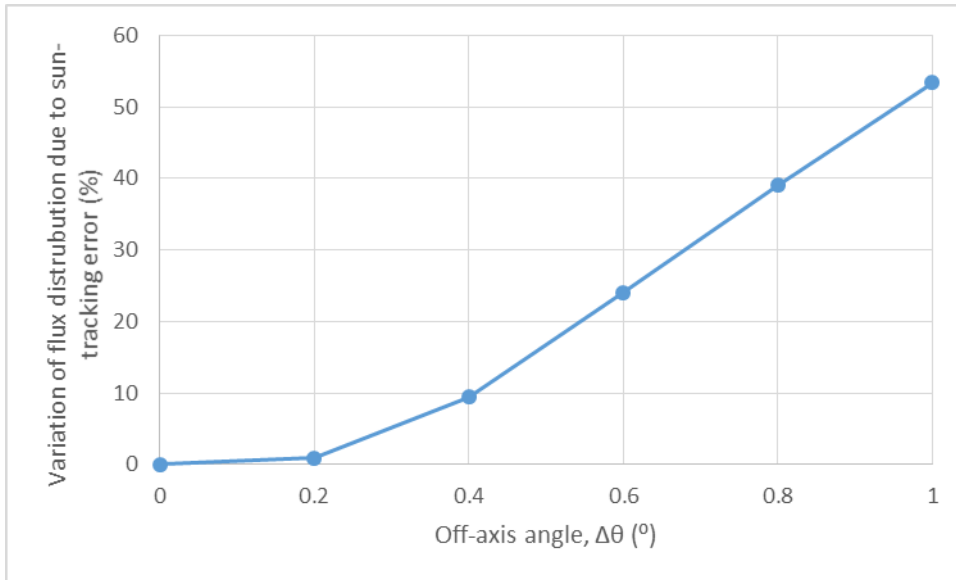


Figure 4.13: The variation in distribution of solar flux in percentage contained in the defined boundary area of $30\text{ mm} \times 30\text{ mm}$ caused by the tracking error versus off-axis angles ($\Delta\theta$) from 0° to 1° .

The tolerance angle of the UHCPV is calculated as a range of acceptable angles with at least 95% energy compared to perfect tracking condition. In Figure 4.14 below, the graph of the percentage of energy incident on the receiver area of $60\text{ mm} \times 60\text{ mm}$ compared to perfect tracking against off-axis angle with a range from -1° to 1° is plotted.

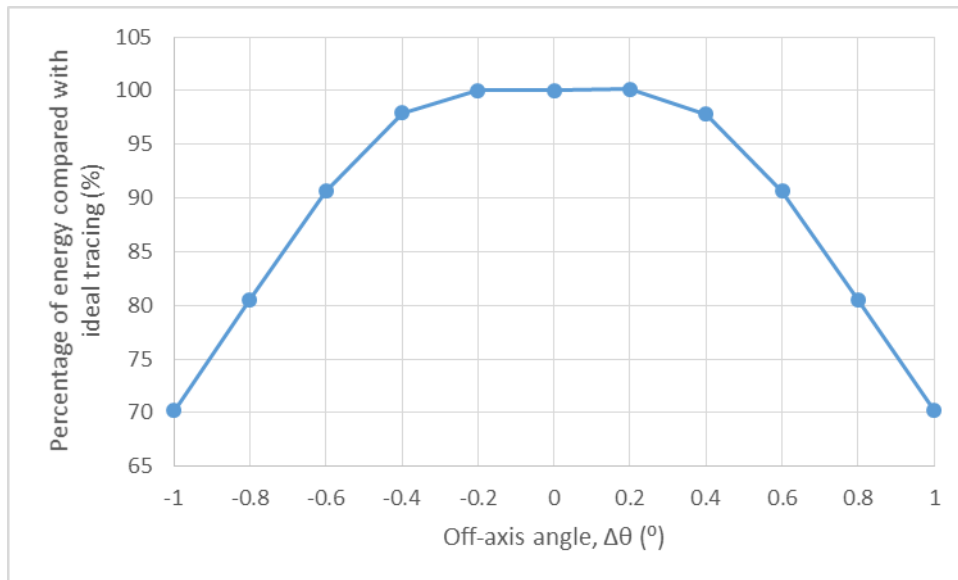


Figure 4.14: Percentage of energy incident on $60\text{ mm} \times 60\text{ mm}$ receiver compared to perfect tracking against off-axis angle with a range from -1° to 1° .

From the graph plotted in Figure 4.14 above, the tolerance angle of the UHCPV system with less than 5% energy loss is determined as 0.44° .

4.7 System performance with focal distance deviation

The focal distance, F is varied from 1150 mm to 1250 mm and the results of the simulated solar irradiation at the exit aperture of the 4 CCPC lens are recorded in Table 4.2 below.

Table 4.2: Characteristics of distribution of solar flux at the 4 CCPC lens at focal distance from 1150 mm to 1250 mm.

| Focal distance (mm) | Average SCR for all CCPC (suns) | Percentage of energy compared to ideal focal distance (%) |
|--------------------------------|--|--|
| 1150 | 1540.60 | 65.08 |
| 1160 | 1754.18 | 74.10 |
| 1170 | 1950.03 | 82.38 |
| 1180 | 2132.88 | 90.10 |
| 1190 | 2284.85 | 96.52 |
| 1200 | 2367.25 | 100.00 |
| 1210 | 2345.63 | 99.12 |
| 1220 | 2234.52 | 94.62 |
| 1230 | 2070.48 | 87.46 |
| 1240 | 1861.78 | 78.65 |
| 1250 | 1653.73 | 69.96 |

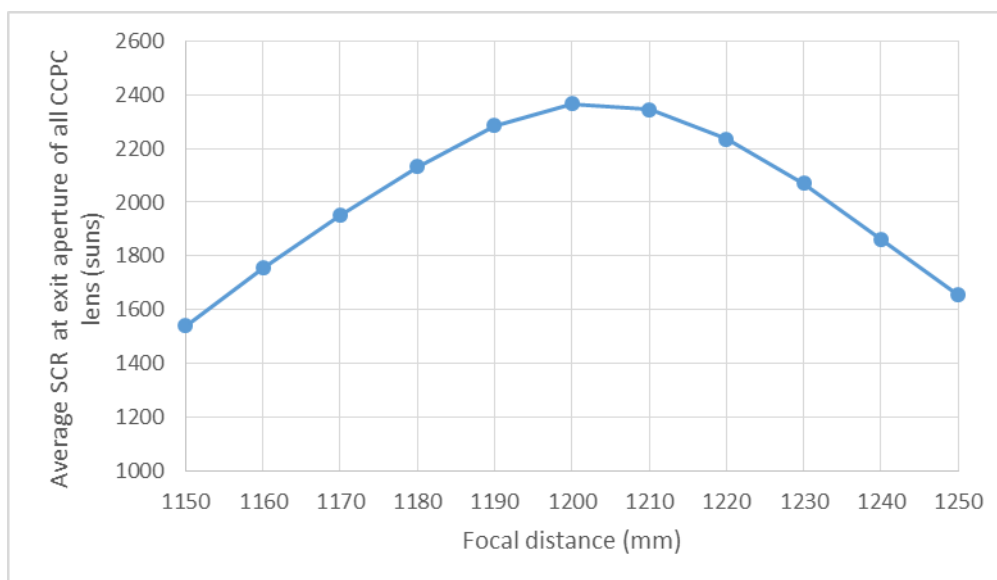


Figure 4.15: Average SCR at exit aperture of all CCPC lens against focal distance.

From Figure 4.15 above, it can be seen that the average SCR at the exit aperture of the CCPC lens exhibits an inverted bell-curve shape as the focal distance is varied from 1150 mm to 1250 mm. This result is expected as the NIDC is designed to focus maximum sunlight to the receiver set at a focal distance of 1200 mm.

The tolerance length of the focal distance deviation is defined as a range of acceptable deviation in focal distance with not more than 5% of energy loss compared with that at ideal focal distance of 1200 mm. In Figure 4.16 below, the graph of the percentage of energy at the CCPC exit aperture compared with that at ideal focal distance against focal distance from 1150 mm to 1250 mm is plotted.

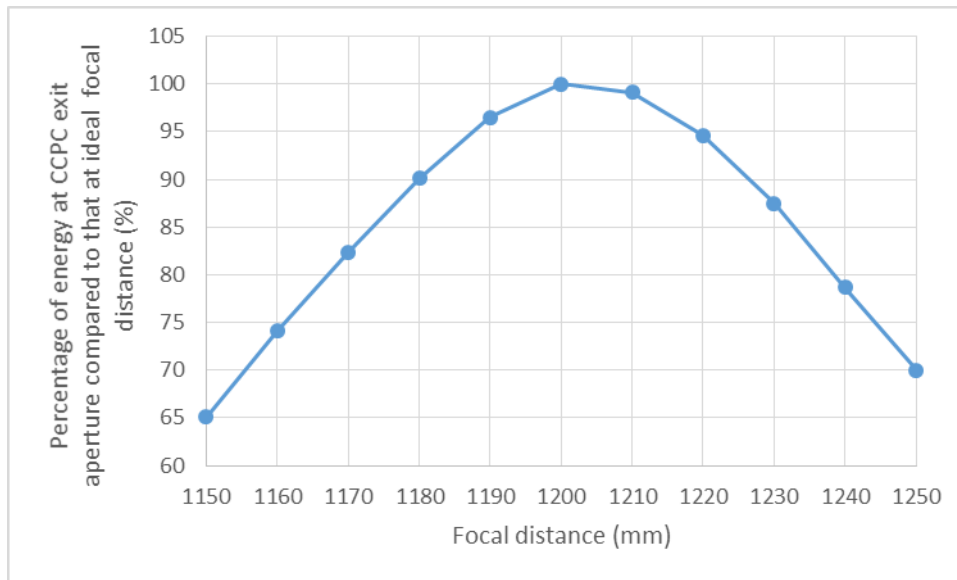


Figure 4.16: Percentage of energy at the CCPC exit aperture compared with that at ideal focal distance against focal distance from 1150 mm to 1250 mm.

From the graph plotted in Figure 4.16 above, it is clear that the tolerance length for focal distance that receives at least 95% of energy is 10 mm. As such, care must be taken when installing the receiver at the focal distance as a 10 mm error will result in 5% energy loss and around 52 suns decrease at the exit aperture of the CCPC lens.

4.8 System performance with slope error of a NIDC quadrant

3 scenarios are simulated using TracePro: a single quadrant is tilted with respect to x-axis and y-axis (Figure 3.5), two adjacent quadrants are tilted with respect to x-axis (Figure 3.6) and two diagonal quadrants are tilted with respect to x-axis and y-axis (Figure 3.7). In the analysis below, a uniformly illuminated area is defined as an area with SCR above 500 suns.

4.8.1 Single quadrant tilted with respect to x-axis and y-axis

The irradiation map and cross-sectional profile of the solar flux on the receiver with a dimension of $60\text{ mm} \times 60\text{ mm}$ are shown in Figure 4.17 to Figure 4.19 as a single quadrant of the NIDC is tilted from 0.2° to 0.6° with respect to both x-axis and y-axis.

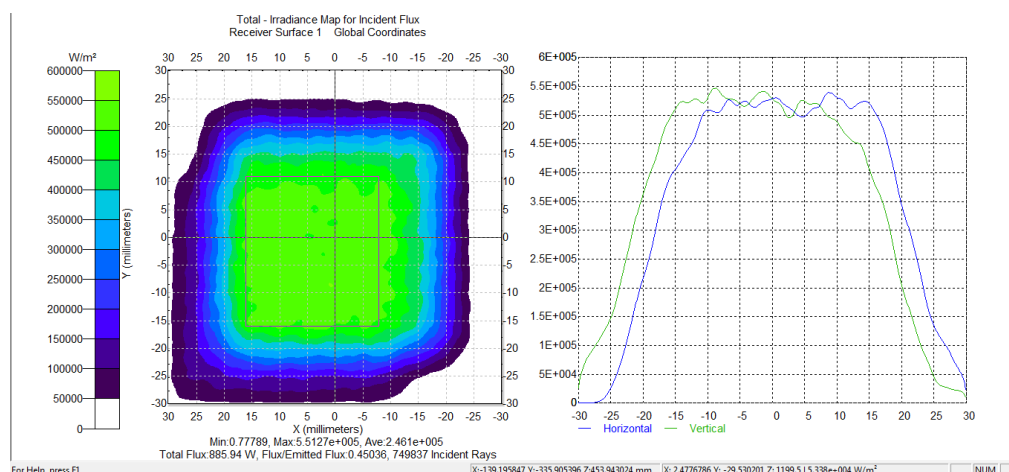


Figure 4.17: Irradiance map and cross-sectional profile for 0.2° tilting angle with respect to x-axis and y-axis.

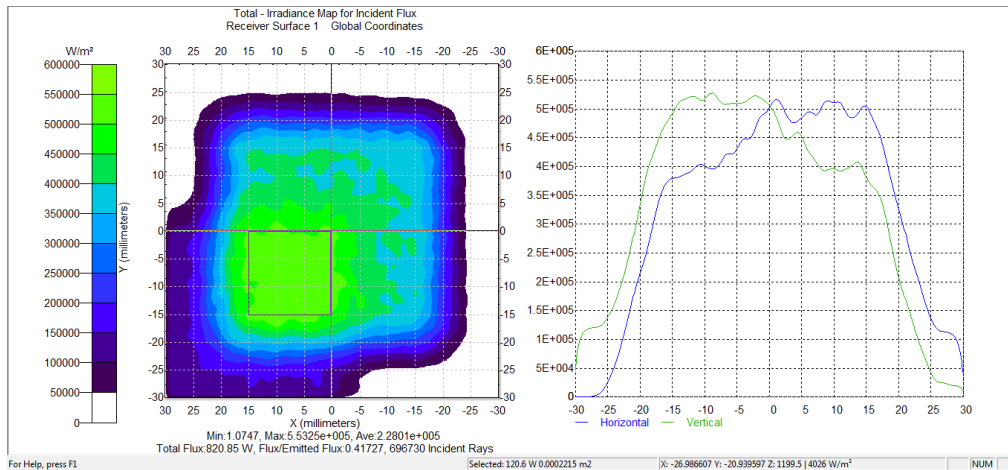


Figure 4.18: Irradiance map and cross-sectional profile for 0.4° tilting angle with respect to x-axis and y-axis.

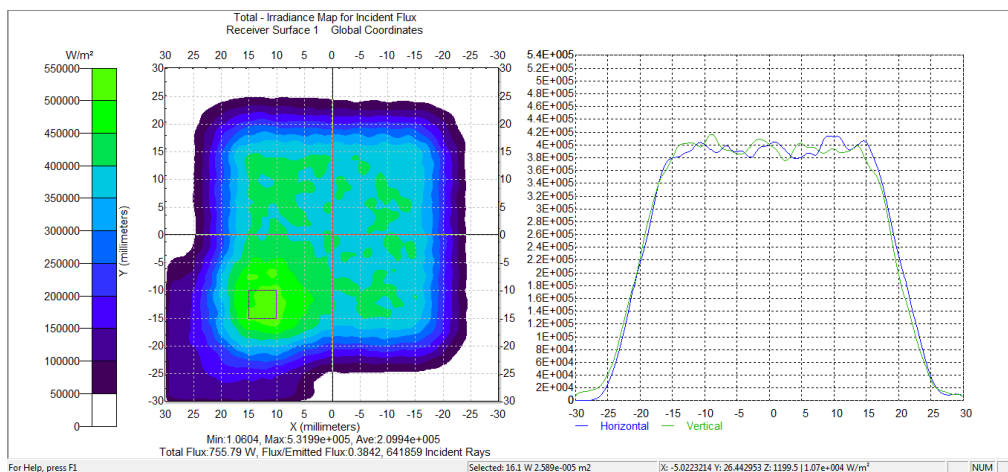


Figure 4.19: Irradiance map and cross-sectional profile for 0.6° tilting angle with respect to x-axis and y-axis.

It can be seen from Figure 4.17 to Figure 4.19 that the average SCR on the receiver decreases and the uniformly illuminated area (over 500 suns) reduces in size against one corner of the receiver as a single quadrant is tilted from 0° to 0.6° with respect to x-axis and y-axis.

4.8.2 Two adjacent quadrants tilted with respect to x-axis

Figure 4.20 to Figure 4.22 show the irradiance map and cross-sectional profile of the solar flux on the receiver with a dimension of $60\text{ mm} \times 60\text{ mm}$ two adjacent quadrant of the NIDC is tilted from 0.2° to 0.6° with respect to x-axis.

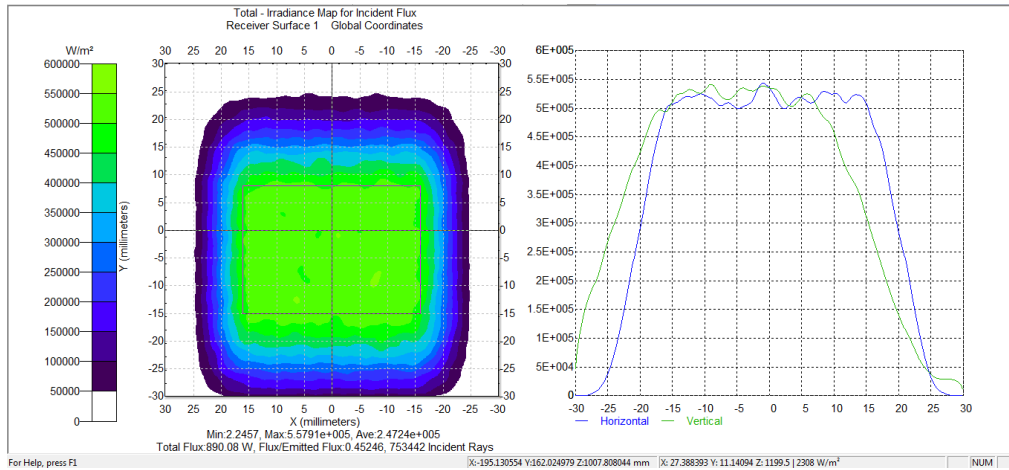


Figure 4.20: Irradiance map and cross-sectional profile for 0.2° tilting angle with respect to x-axis.

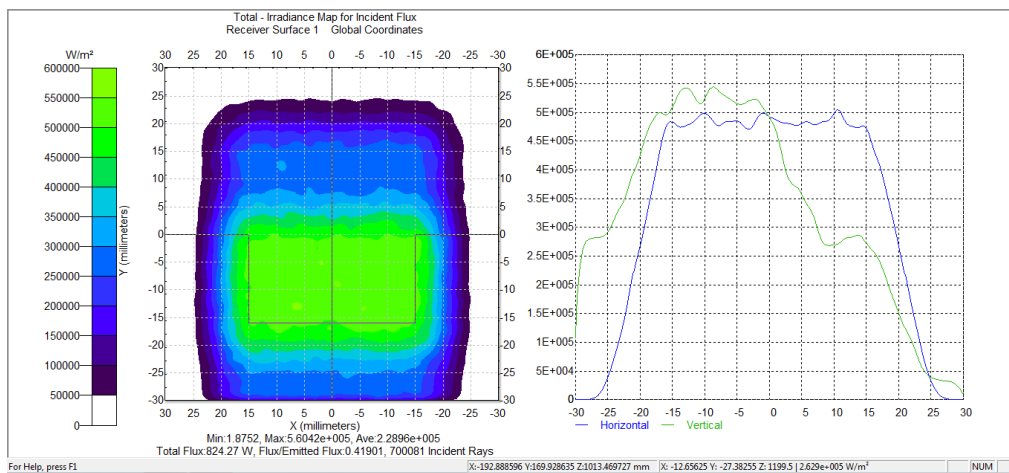


Figure 4.21: Irradiance map and cross-sectional profile for 0.4° tilting angle with respect to x-axis.

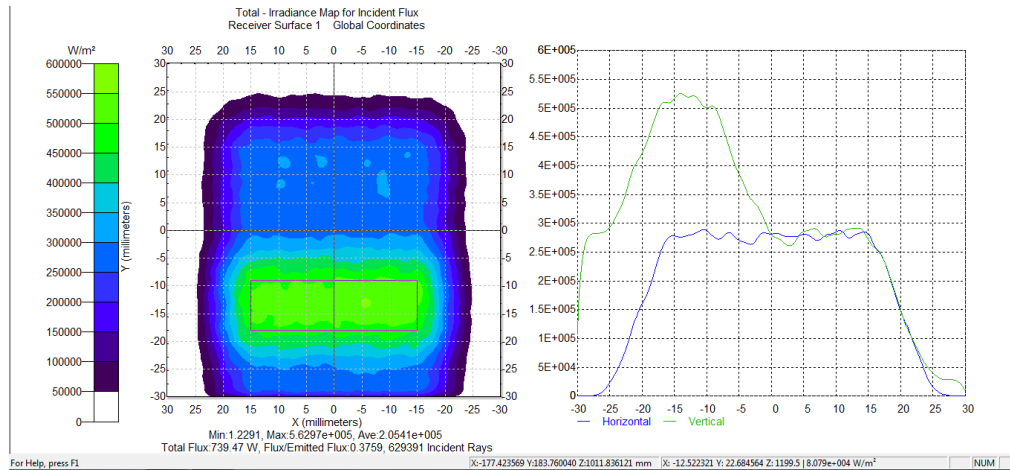


Figure 4.22: Irradiance map and cross-sectional profile for 0.6° tilting angle with respect to x-axis.

It can be seen from Figure 4.21 to Figure 4.22 that the average SCR on the receiver decreases and the uniformly illuminated area (over 500 suns) reduces in size with respect to the y-axis of the receiver as two adjacent quadrant are tilted from 0° to 0.6° with respect to x-axis.

4.8.3 Two diagonal quadrants tilted with respect to x-axis and y-axis

Figure 4.23 to Figure 4.24 show the irradiation map and cross-sectional profile of the solar flux on the receiver with a dimension of $60\text{ mm} \times 60\text{ mm}$ two adjacent quadrant of the NIDC is tilted from 0.2° to 0.4° with respect to x-axis and y-axis.

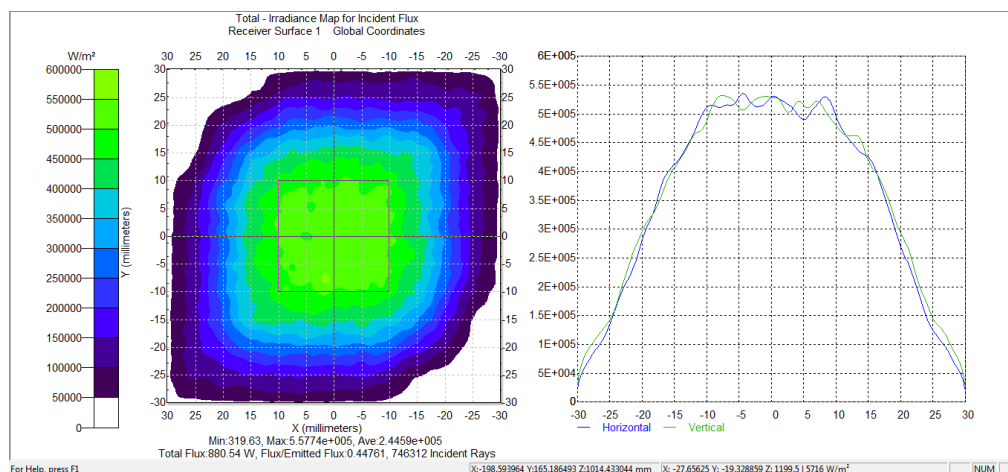


Figure 4.23: Irradiance map and cross-sectional profile for 0.2° tilting angle with respect to x-axis and y-axis.

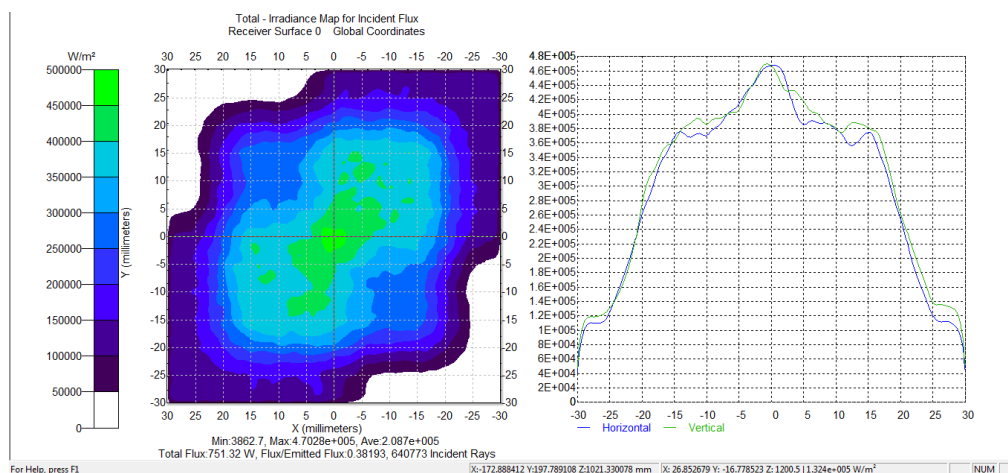


Figure 4.24: Irradiance map and cross-sectional profile for 0.4° tilting angle with respect to x-axis and y-axis.

From Figure 4.23 to Figure 4.24, the average SCR on the receiver decreases and the uniformly illuminated area (over 500 suns) reduces in size against the centre of the receiver as two diagonal quadrant are tilted from 0° to 0.4° with respect to x-axis and y-axis. At a tilting angle of 0.4° , the NIDC can no longer focus the sunlight into a uniformly illuminated area (over 500 suns) on the receiver.

4.8.4 Tolerance angle against slope error

The parameters of the solar flux distribution on the receiver area for all 3 cases are collected. In Figure 4.25 below, the average SCR on the receiver for the 3 cases are plotted against the tilting angle of the NIDC quadrant. On the other hand, the uniformly illuminated area with SCR more than 500 suns for the 3 cases are plotted against the tilting angle of the NIDC quadrant in Figure 4.26.

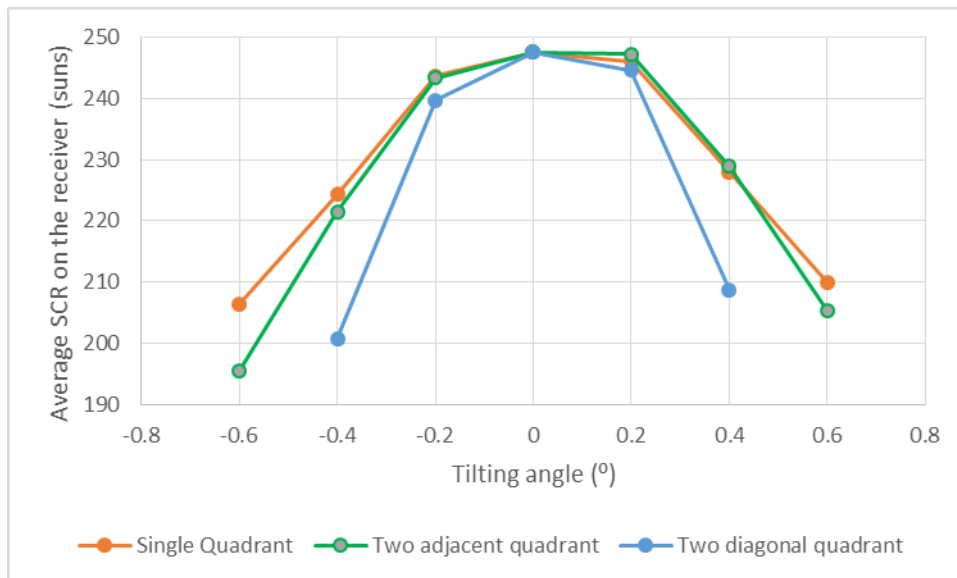


Figure 4.25: Average SCR on the receiver for the 3 cases against the tilting angle of the NIDC quadrant.

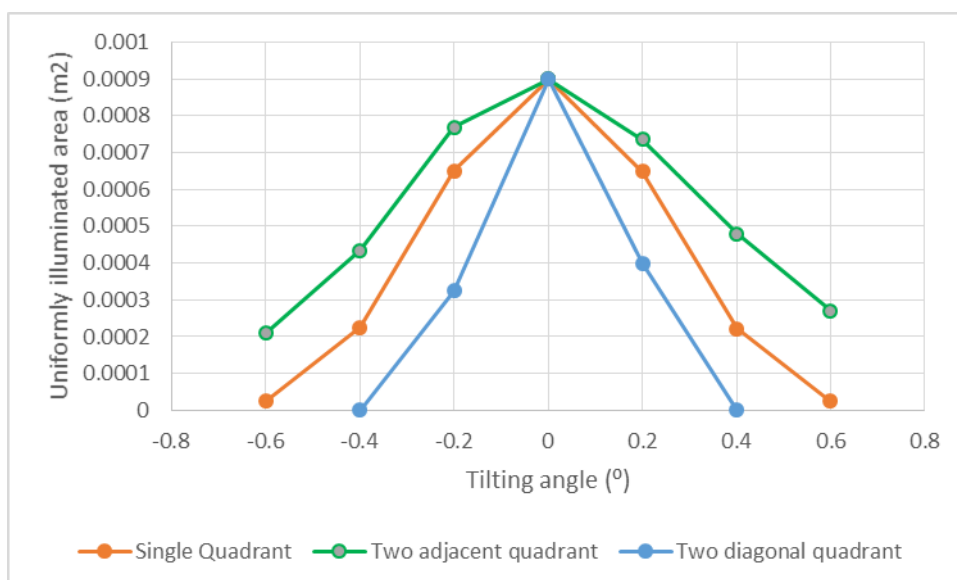


Figure 4.26: Uniformly illuminated area on the receiver for the 3 cases against the tilting angle of the NIDC quadrant.

The tolerance angle against the slope error of the NIDC quadrant is defined as a range of acceptable tilting angles with less than 5% of energy loss compared with ideal condition with no slope error. In Figure 4.27 below, the graph of the percentage of energy at the $60\text{ mm} \times 60\text{ mm}$ receiver with respect to no slope error against the tilting angle of NIDC quadrant is plotted.

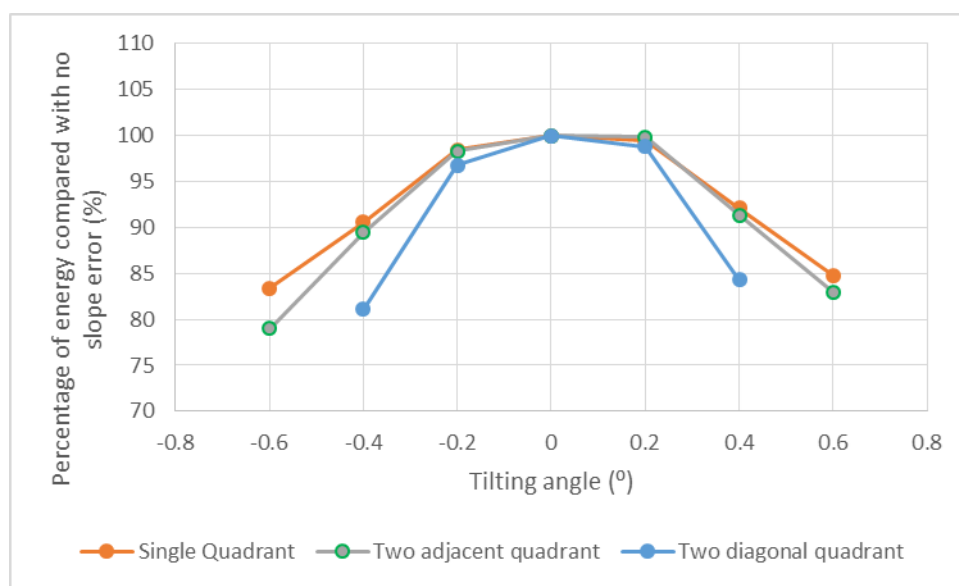


Figure 4.27: Percentage of energy at the $60\text{ mm} \times 60\text{ mm}$ receiver with respect to no slope error against the tilting angle of NIDC quadrant.

From the graph plotted in Figure 4.27 above, a tolerance angle against slope error that receives at least 95% of energy is obtained as 0.3° for the case of single quadrant and two adjacent quadrant tilting while 0.22° is the tolerance angle for the case of two diagonal quadrant tilting.

Moreover, it should be noted that two diagonal quadrant tilting will result in the greatest reduction in average SCR on the receiver, the size of uniformly illuminated area (over 500 suns) and the percentage loss of energy followed by two adjacent quadrant tilting and then single quadrant tilting.

CHAPTER 5

CONCLUSIONS AND RECOMMENDATIONS

5.1 Conclusions

In this project, the optical characteristics of the UHCPV system are investigated using ray-tracing simulation by TracePro. It is found that at 1200 mm focal distance, the SCR on the uniformly illuminated area would be 525 suns. Besides, the optimum receiver area is $60\text{ mm} \times 60\text{ mm}$ as it would only result in a spillage loss of 11.8% at 1200 mm focal distance. The effective SCR, C_{eff} of the UHCPV is simulated to be 2367.85 suns in TracePro. These results are compared then compared to the work done by Wong et al. (2017) and found to be reasonably close.

On the other hand, the tolerance angle resulted by sun-tracking error have been investigated by varying the off-axis angles ($\Delta\theta$) from 0° to 1° . The results show that the uniformly illuminated area shifts from the centre of the receiver without any significant reduction in SCR for off-axis angles ranging from 0° to 0.6° but the SCR drops substantially for off-axis angles ranging from 0.8° to 1° . The tolerance angle of the UHCPV that causes less than 5% of energy loss compared to perfect tracking is determined as 0.44° .

Also, by varying the focal distance at which the receiver is installed, it is found that any deviation greater than 10 mm from the designed 1200 mm focal distance would result in more than 5% of energy loss compared to no error in focal distance.

In addition, the effect of slope error is studied by (1) tilting a single quadrant with respect to x-axis and y-axis, (2) tilting two adjacent quadrants with respect to x-axis and (3) tilting two diagonal quadrants with respect to x-axis and y-axis from 0° to 0.6° . It is found that the average SCR on the receiver as well as the uniformly illuminated area (over 500 suns) reduces as the tilting angle increases. A tolerance angle against slope error that receives at least 95% of energy is obtained as 0.3° for the case of single quadrant and two adjacent quadrant tilting while 0.22° is the tolerance angle for the case of two diagonal quadrant tilting.

In conclusion, the simulated solar flux distribution in TracePro have shown a high concentration ratio at the receiver plane with reasonably good uniformity of solar irradiance. The tolerance angle against sun-tracking error, focal distance deviation and slope error are obtained.

5.2 Recommendations for future work

Further work can be done by simulating the slope error of individual mirrors in the model. Also, the resolution of the irradiance map can be increased by simulating more rays using TracePro. The actual focused image at the receiver obtained by Khor (2019) can be digitised and compared to the TracePro results as well.

REFERENCES

Algora, C. and Rey-Stolle, I., 2016. *Handbook of Concentrator Photovoltaic Technology*. Hoboken: John Wiley & Sons Inc.

Chong, K.K., Yew, T.K., Wong, C.W., Tan, M.H., Tan, W.C. and Lim, B.H., 2017. Dense-array concentrator photovoltaic prototype using non-imaging dish concentrator and an array of cross compound parabolic concentrators. *Applied Energy*, [e-journal] 204, pp.898–911. Available at: <<http://dx.doi.org/10.1016/j.apenergy.2017.03.108>> [Accessed at 24 April 2020]

European Photovoltaic Technology Platform, 2011. *A Strategic Research Agenda for Photovoltaic Solar Energy Technology*, Edition 2 [online]. Available at: <www.eupvplatform.org/publications/strategic-research-agenda-implementation-plan.html> [Accessed at 26 April 2020]

Energy Information Administration, 2019. *EIA projects nearly 50% increase in world energy usage by 2050, led by growth in Asia*. [online] Washington DC, US: EIA. Available at: <<https://www.eia.gov/todayinenergy/detail.php?id=41433>> [Accessed at 24 April 2020]

George, M., Pandey, A. K., Nasrudin Rahim and Siadur, R., 2018. Recent Studies in Concentrated Photovoltaic System (CPV): A Review. In: *5th IET International Conference on Clean Energy and Technology (CEAT2018). Malaysia, 5-6 September 2018*. Kuala Lumpur, Malaysia: IET. pp. 1-8. Available at: <<https://ieeexplore.ieee.org/document/8651218>> [Accessed at 25 April 2020]

Khor, C.M., 2019. *Electrical Characteristics Analysis of Ultra-High Solar Concentrator System*. Undergraduate. Universiti Tunku Abdul Rahman.

Lee, P.S., Wong, C.W, Tan, M.H. and Chong, K.K. (2020). Comprehensive analysis on assembly of dielectric filled crossed compound parabolic concentrator and concentrator photovoltaic module. *Applied Optics*, 59(14), pp. 4557-4565 [online]. Available at: <https://www.researchgate.net/publication/340390535_Comprehensive_analysis_on_assembly_of_dielectricfilled_crossed_compound_parabolic_concentrator_andconcentrator_photovoltaic_module> [Accessed at 10 September 2020].

Li, G., Xuan, Q., Pei, G., Su, Y. and Ji, J. (2018). Effect of non-uniform illumination and temperature distribution on concentrating solar cell - A review. *Energy*, 144, pp. 1119-1136 [online]. Available at: <<https://www.sciencedirect.com/science/article/abs/pii/S0360544217321059>> [Accessed at 26 April 2020]

Philipps, S.P., Bett, A.W., Horowitz, K. and Kurtz, S., 2015. *Current Status of Concentrator Photovoltaic (CPV) Technology*. [pdf] Germany and US, Fraunhofer ISE and NREL. pp. 1–25. Available at: <<http://www.ise.fraunhofer.de/en/publications/veroeffentlichungen-pdf-dateien-en/studien-und-konzeptpapiere/current-status-of-concentrator-photovoltaic-cpv-technology.pdf>> [Accessed at 24 April 2020]

REN21, 2019. *Renewables 2019 Global Status Report*. [online] Paris, France: REN21 Secretariat. Available at: <<https://wedocs.unep.org/bitstream/handle/20.500.11822/28496/REN2019.pdf?sequence=1&isAllowed=y>> [Accessed at 23 April 2020]

Spectrolab, 2010. *CCA 100 C3MJ Concentrator Cell Assembly*. California, US: Spectrolab. Available at: <<http://www.spectrolab.com/DataSheets/PV/CPV/C3MJ%20CCA-100%20data%20sheet%2020100828.pdf>> [Accessed at 25 April 2020]

United Nations, 2019. *World Population Prospects 2019: Highlights*. [online] New York City, US: UN. Available at: <<https://www.un.org/development/desa/publications/world-population-prospects-2019-highlights.html>> [Accessed 24 April 2020]

Weisenharth, M., Anton, I. and Bett, A.W., 2018. Challenges in the design of concentrator photovoltaic (CPV) modules to achieve highest efficiencies. *Applied Physics Reviews*, [e-journal] 5(4), pp.041601. Available at: <https://pdfs.semanticscholar.org/36d9/687f9ef4184b6e4554fa840254d805280ead.pdf?_ga=2.27044084.87698126.1587614251-950951757.1587614251> [Accessed at 24 April 2020]

Wong, C., Yew, T., Chong, K., Tan, W., Tan, M. and Lim, B., 2017. Design optimization of ultra-high concentrator photovoltaic system using two-stage non-imaging solar concentrator. *IOP Conference Series: Earth and Environmental Science*, [online] 93. Available at: <<https://iopscience.iop.org/article/10.1088/1755-1315/93/1/012012/pdf>>. [Accessed at 24 April 2020]